Simulation of High-velocity Penetration for Rigid Projectile into Plain Concrete Target using Discrete Element Method

Yu ZHOU

Thesis submitted to the faculty of

Virginia Polytechnic Institute and State University

in partial fulfillment of the requirements for the degree of

Master of Science

In

Civil Engineering

Linbing Wang, Chair
Gerardo W. Flintsch
Antoine G. Hobeika

February 4, 2009

Blacksburg, Virginia

Keywords: Penetration, DEM, Simulation, Calibration

Simulation of High-velocity Penetration for Rigid Projectile into Plain Concrete Target using Discrete Element Method

Yu ZHOU

(ABSTRACT)

Penetration of high velocity is of concern for both civilian and military research for decades, and computerized simulation is the scholar's focus in recent years. This study presents a study on the Discrete Element Method (DEM) simulation of plain concrete target's behavior under high-velocity penetration of rigid projectile.

In this thesis, different types of research works including empirical, analytical and numerical methods in penetration by the previous scholars were carefully reviewed. A DEM-based concrete model was established by using software PFC3D. The major micro-variables of the simulation program were calibrated according to the required macro-mechanical parameters. Meanwhile, their correlations within the concrete range were studied, with the sensitivity analysis and the corresponding regression equations.

With the established digital concrete model, penetration simulation tests were carried out. The results of penetration depth versus impact velocity were compared with the experimental and empirical calculated results from Forrestal's work in 1994. A good agreement was obtained. Some other simulation studies, like projectile mass, geometry, penetrating acceleration, concrete response stress, strain, and strain-rate were also conducted to study the constitutive properties in this thesis.

This thesis is dedicated to my parents Jianguo ZHOU and Xiaoqin HE

ACKNOWLEDGEMENT

The author wants to thank his advisor, Dr. Linbing Wang for his support and patient supervision. His valuable and constructive advice and comments are greatly appreciated.

The author also wants to thank his advisory committee members, Dr. Gerardo W. Flintsch, and Dr. Antoine G. Hobeika, for their valuable advices and support during coursework and thesis preparation.

The author would like to thank his colleagues and friends for their help both in and out of office and laboratory.

The research was made possible with the support from the Department of Civil and Environmental Engineering and VTTI of Virginia Tech.

TABLE OF CONTENT

LIST OF FIGURES

LIST OF TABLES

Chapter 1. Introduction

1.1. Research Background

Penetration of high velocity projectiles into concrete targets is a concern of both civilian and military research. The earliest study of penetration mechanics can be traced back to 300 years ago; however, it is World War II that triggered the systematic focus into this specialty.

Numerical simulation of penetration comes with the application of Finite Element Method (FEM) and Discrete Element Method (DEM). FEM has been used widely since the 1970s, while DEM only became the popular since 1990s. There is not much study of DEM application in the penetration research.

1.2. Research Objectives

The objective of this thesis is to make use of DEM to simulate the normal high-speed penetration into semi-infinite plain concrete target. Detailed purposes are:

1. Build up a DEM digital concrete model with PFC3D.

2. Calibrate the key microscopic variables according to the macroscopic properties, conduct the sensitivity analysis, and get the correlation regression equations.

3. Use the calibrated digital concrete model to simulate the test of normal high-speed penetration.

4. Carry out a vast quantity of simulation tests to study the correlation between the penetration depth and other key factors, such as the impact velocity and the shape of projectile.

5. Compare simulation results with experimental results and those from empirical theory, through the use of diagrams representing depth-velocity.

6. Study the constitutive relation under different dynamic conditions

1.3. Research tasks and organization

This thesis is organized into five chapters:

Chapter 1 describes the background of the study, clarifies the research objective, and explains the organization of this thesis.

Chapter 2 presents the review of relevant literature for this study. The first part introduces the basics and the key parameters of the penetration study, while the second part focuses on several methodologies for penetration study completed by previous scholars, which are classified into empirical, analytical, and numerical methods.

Chapter 3 introduces the simulation method applied in this report. PFC3D is the software used for the modeling, while DEM was the theory behind it. The fundamental rules for DEM (force-displacement law, motion law, and contact models) are explained first. Then the sample key variables setting for both projectile and target are listed in the next section, followed by the corresponding sample digital model.

Chapter 4 is about one of the major work completed in this thesis. The individual and multi effect of the major micro-variables in PFC programming have been studied, provided with the sensitivity analysis and the corresponding regression equations. Based on these principles discovered, a calibration has been conducted for the digital concrete material to obtain the required mechanical property.

On the basis of the calibrated projectile and target model, a penetration simulation model is presented and in Chapter 5. With this model, series of simulation test have been conducted. Not only the visualization of the whole process is shown,

but also the history record of monitored internal variables have been kept. Among them, the penetration depth-impact velocity correlation has been used to validated the established digital model through the comparison with the experiment and empirical results done by the previous work. And the stress-strain correlation have been studied, which shows that the mechanical property of concrete is rather a rate-dependent term not static.

Chapter 6 summarizes the findings and limitations of this thesis, and provides recommendations for further study.

Chapter 2. Literature Review

2.1. Penetration Introduction

2.1.1. Basics about penetration and the focus of this thesis

Due to the various impact conditions and target properties, the injection of a projectile into a target can be divided into different response types, as seen in Figure 2-1. Among them, the normal impact strike type receives the most concern. There are three possible results (Cargile 1999) depending on the impact energy on the target:

1. Impact- the strike only forms an impact crater;

2. Deep Penetration- the projectile goes over the crater, forms a tunnel, and is finally embedded in the target;

3. Perforation- the projectile pierces the target of finite thickness, while the whole process creates an impact crater, a tunnel, and an exit crater.

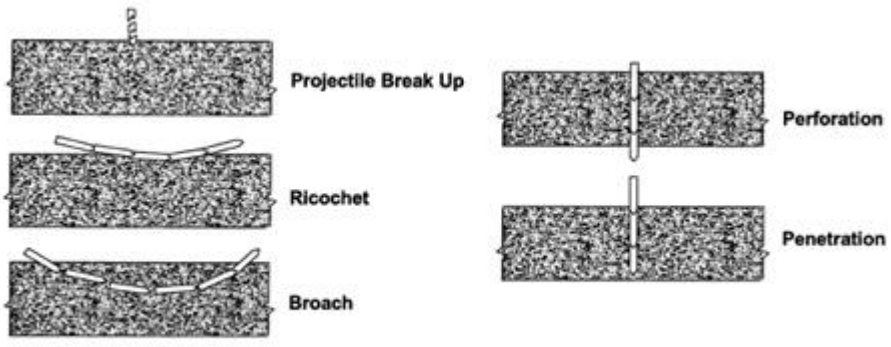

Figure 2-1. Projectile response after impact (Cargile 1999)

Most research focuses on deep penetration (usually idealizing the target as a semi-infinite body in the theoretical study), which is dominated by severe compaction, shear, and tension. The principal force takes effect at the resistance around the

projectile nose, while the extremely high stress in the neighboring area decreases rapidly away from the cavity.

Other special types of impact are considered non-ideal, such as ricochet, broach (due to oblique impact), breaking up (due to low strength of penetrator), yaw, moving target, rotating or tumbling, etc. These types also include phenomenon as detailed in Goldsmith's summary review (Goldsmith 1999). Considered, however, these special cases are not.

2.1.2. Key parameters for penetration

There are many important characteristics of both target and projectile that affect penetration results. These features determine the constitutive relationship of both entities. Below are some typical parameters for penetration research and their typical values discovered in the past studies.

For the target:

1. Dimension: semi-infinite (applied to deep penetration); Finite (applied to perforation, especially when people are interested in the phase of exit crater).

2. Material type: metal; composite (such as concrete); geomaterial (such as rock, soil, frozen soil, sediment, and etc), ice, and layered material.

3. Mechanical property, which is related with the material type: elastic modulus, poisson's ratio, and strength (compressive and tensile).

For the projectile:

1. Impact velocity;

2. Impact angle to the target (normal, oblique);

3. Mass;

4. Strength (rigid, deformable);

4. Geometry (tail diameter, nose shape as seen in Figure 2-2).

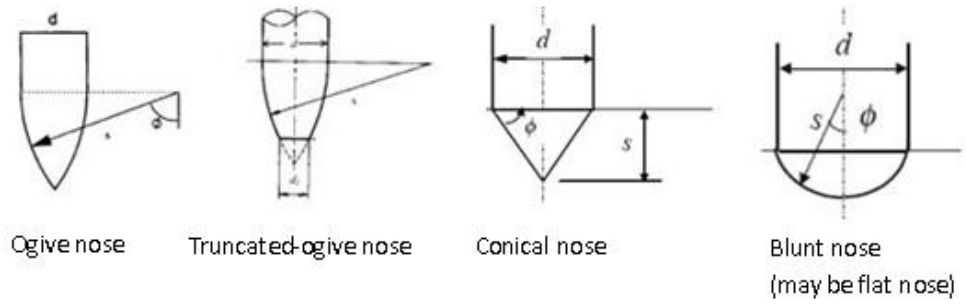

Figure 2-2. The geometry of projectile nose shape (Chen and Li 2002)

2.2. Methodologies for penetration study

F. E. Heuze (Heuze 1990) provided a comprehensive and valuable summary of the penetration studies conducted before 1990. Heuze's summary focused on geological material, especially rocks, and classified all the methodologies into the empirical, the analytical, and the numerical simulation methods. It covered nearly all the important methods on penetration research. Due to the similarity of constituents and mechanics between concrete and rocks, his classification system is utilized in this study.

The applications of different methodologies vary according to the research range and depth. The empirical method provides the simplest and easiest way to obtain the macroscopic factors, such as penetration depth; the analytical method can provide answers for not only the direct observable parameters, but also some other properties, such as stress and strain relationship; and the numerical simulation could offer the detailed description of the entire penetration process from all aspects, yet sometimes not precisely consistent with the experimental observations.

In addition to describing the existing models, Heuze (Heuze 1990) also compared the different methods. His conclusions drawn on the overview of the whole

study area include:

1. Cracks and joints are ubiquitous and damage characterization should be incorporated in the modeling and simulation;

2. Shear strength is sensitive to the mean stress, and yielding strength should be mean stress dependent;

3. Post-fracture properties of the broken material are also essential and the interaction among the fragments should be considered;

4. The internal friction angle of the target is more important than its cohesive strength in controlling penetration.

2.2.1. Empirical methods

The Empirical methods may be the oldest and most direct. They are based on the experimental data, and usually apply mathematical tools like regression to get an empirical relation. The wide use of empirical methods is due to their simplicity and good correlation with test results, which enables a quick first approximation and comparison to other methods.

2.2.1.1. Normal penetration case studies

M.E.Backman (Backman and Goldsmith 1978) included some examples of empirical formulae developed by the scholars in the 19th century as shown below. It is noticeable that some typical parameters are concern of different researchers, such as P - penetration depth; m – projectile mass; v_0 - the impact velocity; θ - obliquity and the type of target and its thickness h_0; D - projectile tail diameter; E_0 - required perforation energy, ρ_t - target density; a_i - arbitrary constants.

Morin (1833)'s equation

$$P / D = 2mv_0^2 / a_1 \pi D^3 \qquad \textbf{2-1}$$

Dideon's equation

$$P / D = a_2 \rho_t \ln(1 + a_3 v_0^{\,2}) \qquad \textbf{2-2}$$

Helie's equation

$$P / D = (4.608m / a_4 D^3 \pi \rho_t) \log_{10}(1 + a_5 v_0^{\,2}) \qquad \textbf{2-3}$$

where

P - penetration depth;

m – projectile mass;

v_0 - the impact velocity;

θ - obliquity and the type of target and its thickness h_0;

D - projectile tail diameter;

E_0 - required perforation energy,

ρ_t - target density;

a_i - arbitrary constants.

All of these equations are based on the semi-infinite (SI) target.

The Army's Waterways Experiment Station (WES), Vicksburg (Bernard 1977; Bernard 1978) developed their formulae for penetration research, which is another important reference in the last 20 years. Its theory incorporate a characteristic parameter, Rock Quality Designation (RQD), the percent of total core length made up of pieces at least 4 inches long. This parameter needs to be back-calculated from the penetration tests. A typical penetration depth equation is shown below.

$$Z = \frac{M}{A}\frac{N_{rc}}{\rho}[\frac{V}{3}\frac{\rho^{1/2}}{\sigma_{cr}{}^{1/2}} - \frac{4}{9}\ln(1+\frac{3}{4}V\frac{\rho^{1/2}}{\sigma_{cr}{}^{1/2}})] \qquad \textbf{2-4}$$

where

N_{rc} - The projectile nose performance coefficient

$$\begin{cases} N_{rc} = 0.863[\dfrac{4(CRH)^2}{4CRH-1}]^{1/4} & for \quad ogive\_nose \\ N_{rc} = 0.805(\sin\eta_c)^{-1/2} & for \quad cone\_nose \end{cases}$$

$\sigma_{cr} = \sigma_c(RQD/100)^{0.2}$

M - the concrete mass

σ_{cr} - the unconfined compressive strength

η_c - the cone half-angle

Rock Quality Designation (RQD), also used in concrete, is calculated as the percent of total core length made up of pieces at least 4 inches long. Compared to Q, the shortcoming of RQD is that its magnitude is dominated by horizontal cracks.

Another depth formula was developed in 1992 by WES.

$$X = \frac{222 * N * W * V^{1.8}}{D^{1.8} * f_c{}'^{0.5}} + D; \text{ for X>2D} \qquad \textbf{2-5}$$

where

$N = 0.72 + 0.25(CRH - 0.25)^{0.5}$

X - penetration depth, inch

f_c' - compressive strength of concrete, psi

N - nose shape factor or nose performance coefficient

W - projectile weight, lb

D - projectile diameter, inch

V - impact velocity/1000, fps

Sandia National Laboratories (SNL) in Albuquerque, New Mexico plays a very important part in the penetration study. Among the researchers there, Young, C.W and his colleagues (Young 1967; Young 1972; Schoof, et al. 1989; Young 1998) developed their empirical models and continued their work into diverse kinds of conditions. In 1997, Young summarized his previous work done in penetration, covered in his paper all prediction equations he developed for different penetrator nose shape (ogive, conic, blunted), impact velocities (<200fps, ≥200fps), types of targets (rock, concrete, ice, and the layered target). Young's equations have been incorporated into different program codes, like SAMPLL code and MOLE code, which enable efficient penetration modeling.

The Penetration Depth equations for uniform layer or half space of concrete

$$\begin{cases} D = 0.3SN(W/A)^{0.7}\ln(1+2V^2 10^{-5}) \text{ , } for \quad V < 200\ fps \\ D = 0.00178SN(W/A)^{0.7}(V-100) \text{ , } for \quad V \geq 200\ fps \end{cases} \qquad \textbf{2-6}$$

where

W - weight of penetrator, lbs

A - cross sectional area, m^2

The depth equations above should be multiplied by the scaling term K (geometric scale factor), when the weight is lower than 400lbs.

$K = 0.4(W)^{0.15}$, when W<400lbs

Young applied in his theory two of the most widely used parameters, N and S, which represent the properties of penetrator (the shape of the nose) and target (material) respectively. He developed his own formula definition of these two parameters (Young 1997); however, other researchers may have different definitions for them. Young (Young 1972) also extended his work into layered structures, which considered both the cratering (entry) and spalling (exit) steps.

Forrestal and his colleagues' work (Forrestal, et al. 1994) have been seen as one of the most important achievement for penetration in recent 20 years and referred frequently for comparison in later research. Unlike the direct depth-velocity relation provided by other scholars, they based their study on Cavity expansion theory (CET) to establish a model for ogive-nose projectile. Their method could also be called semi-analytical method, with both analytical and empirical technique.

With CET, Forrestal transforms the force expression for the nose resistance $F = \pi a^2(\tau_0 A + NB\rho V^2)$ from their previous work (Forrestal and Luk 1992). This is done in order to separate f_c', the unconfined compressive strength, which is easily obtained and can well describe the mechanical property of concrete.

$$\begin{cases} F = cz & ,0 < z < 4a \\ F = \pi a^2(Sf_c' + N\rho V^2) & ,4a < z < P \end{cases} \qquad \textbf{2-7}$$

where

a – shank radius

$$c = \frac{\pi a}{4}(Sf_c' + N\rho V_1^2)$$

V_1 - the rigid-body projectile velocity when the crater phase starts at z= 4a;

$$V_1^2 = \frac{mV_s^2 - 4\pi a^3 R}{m + 4\pi a^3 N\rho}$$

V_s - the striking velocity.

$$N = \frac{8\psi - 1}{24\psi^2}$$

ψ - the caliber-radius-head

ρ - the concrete density

The force expression is integrated with Newton's law to get the final depth:

$$P = \frac{m}{2\pi a^2 \rho N} \ln(1 + \frac{N\rho V_1^2}{Sf_c'}) + 4a, \text{ P>4a} \qquad \text{2-8}$$

For the S-number, other than Young, Forrestal used the experimental method to get the average, as shown below (every term in the right can be attained from tests).

$$S = \frac{N\rho V_s^2}{f'_c} \frac{1}{(1 + \frac{4\pi a^3 N\rho}{m}) \exp[\frac{2\pi a^2 (P - 4a) N\rho}{m}] - 1}, \text{ dimensionless constant}$$

Forrestal and his colleagues continued their work by applying this model to a special case of solid-rod projectile (Forrestal, et al. 1996; Frew, et al. 1998), and refining the theory (Forrestal, et al. 2003) by taking R=Sf_c' as the target strength parameter. The work of his colleagues, Farmer and Frew (Frew, et al. 2001), concluded that unconfined Compressive strength f_c' is rather an index depending on sample size than a material property. Therefore, the R-number is the necessary constant achieved from the average of the tests..

$$R = \frac{N\rho V_s^2}{(1 + \frac{4\pi a^3 N\rho}{m}) \exp[\frac{2\pi a^2 (P - 4a) N\rho}{m}] - 1} \qquad \textbf{2-9}$$

And the final penetration depth equation could be modified to

$$P = \frac{mV_s^2}{2\pi a^2 R} + 2a \qquad \textbf{2-10}$$

where

$$w^2 = c/m$$

$$c = \pi aR/4$$

$$t_1 = \frac{\cos^{-1}(V_1/V_s)}{(\pi aR/4m)^{1/2}}$$

$$V_1^2 = V_s^2 - \frac{\pi a^3 R}{m}$$

2.2.1.2. Special penetration cases study

Based on the model developed by Forrestal, Gomez (Gomez and Shukla 2001) explored multiple impact penetration by adding the shot number factor to the target constant S, and built up the formulae in this condition. Observation in this whole penetration process is similar to the single impact model, forming a crater at the surface and then tunneling into the target. The only difference is the crater depth is slightly deeper, which changes z=4a to z=5a. Below are the equations taking into account of this change:

$$P = \frac{m}{2\pi a^2 \rho N}\ln\left(1 + \frac{N\rho V_1^2}{Sf'_c}\right) + 5a \qquad \textbf{2-11}$$

where

$$V_1^2 = \frac{mV_s^2 - 5\pi a^3 Sf'_c}{m + 5\pi a^3 N\rho}$$

What should be noticed is the S factor, which evolves with the shot number.

$$S_n = S_1(-0.04465\ln(n)+1)$$

n - the shot number

S_1 - the factor for the initial shot into the undamaged target

Since Forrestal's work only considered the ogive-nose shape, Qian and Yang (Qian, et al. 2000) extended their theory to include the truncated-ogive-nose projectile. Their work introduced two empirical constants, resistance coefficient c', which takes into account the truncation effect, and impact crater depth ka, in addition to the equations for the normal penetrator.

$$P = \frac{m}{2\pi a^2 \rho N c'}\ln(1+\frac{N\rho V_1^2}{Sf'_c}) + ka, P > ka \qquad \textbf{2-12}$$

where

k=3-5, thickness constant of the spalling region

$c' = 1 + K\frac{A'}{A} = 1 + K\frac{r^2}{a^2}$, resistance coefficient

$K = \frac{a^2}{r^2}(c'-1)$, the resistance ratio of truncated-ogive-nose over ogive-nose.

A - cross-section areas of the shank;

A' - end face area of the truncated part

Teland and his colleagues (Teland and Sjol 2004) are also interested in this area but tried not to introduce the additional empirical constants like Qian. The modification they did to the Forrestal's theory is to introduce a non-dimensional depth parameter X to do the derivation. They also differentiated the force on the penetrator into two parts: the one on the nose, the other on the flat section; and defined the tunneling at depth X_1, which does not equals Forrestal's X_1=2 but a parameter, after

the crater step. And their work can also be applied to different nose shapes.

$$X_p = \frac{2}{\pi}\frac{M}{N}\ln\left[\frac{(1-\frac{\pi}{4}\frac{R^2}{M}X_1)\frac{V_0^2}{S}+\frac{M}{N}-\frac{\pi}{4}R^2X_1}{\frac{M}{N}+\frac{\pi}{4}X_1}\right]+X_1 \qquad \textbf{2-13}$$

where

$$N=\begin{cases} N_0+R^2\left[\dfrac{6(2\psi-1)^2+8R(2\psi-1)+3R^2}{24\psi^2}\right] & , for \quad ogive\_nose \\ 1-\left[\dfrac{1-R^4}{8\psi^2}\right] & , for \quad blunt\_nose \end{cases}$$

$X_i = x_i / d$, relative depth

$$\begin{cases} X_1=\sqrt{\psi(1-R)-\dfrac{1}{4}(1-R)^2} & , for\_ogive\_nose \\ X_1=\sqrt{\psi^2-\dfrac{R^2}{4}}-\sqrt{\psi^2-\dfrac{1}{4}} & , for\_blunt\_nose \end{cases}$$

x_i - the real penetration depth

d – projectile tail diameter

2.2.2. Analytical methods

T he analytical method is another important type of approach utilized in penetration studies. It utilizes the principle of mechanics to analyze the physical property of target material and proposes corresponding models. This type of approach is a more fundamental method, because it is able to offer a closed-form solution, usually based on the conservation and balance laws, and comprised of algebraic relation, like ordinary differential equations. The models established on this analytical solution can be considered as a foundation for further experiment and theory study.

Differential Area Force Law (DAFL) is a typical analytical method, proposed

by AVCO Corporation in the early 1970s (Henderson 1976). The basic idea of this method is to divide the projectile longitudinally and circumferentially into meshes. Thus stresses are described for different areas and summed up. The limitation of this method is that seven of the nine critical parameters need to be determined by empirical regression, which lowers the utilization.

Currently, CET is the most widely used analytical model. And the whole theorem can be grouped into two main subcategories based on the cavity types: spherical cavity expansion theory (SCET), and cylindrical cavity expansion theory (CCET).It was first introduced by Bishop (1945) (Bishop, et al. 1945) with the quasi-static model in his research of one-dimensional motion of target response. Despite its limitation of only being valid for normal impact, this type of method is still used in penetration analytical study after 40 years

After the introduction of the quasi-static model by Bishop, Hopkins (1960) not only made a summarization of previous works, but also developed a dynamic CET for incompressible target material, which had been widely used even now. His theorems assume the penetration resistance to be the sum of the shear resistance and the inertial effects of projectile movement in the target (dynamic resistance). The basic idea of both theorems is the relation between the radial stress and the radial velocity:

$$\sigma_r = A * Y + B * \rho V^2 \qquad \textbf{2-14}$$

where A and B depend on the mechanical properties of the solid around the cavity (r is its density, and Y its yield strength).

This stress can be summed up as the resisting force, which is integrated to calculate the acceleration, velocity, and depth, which all originated from Newton's second law. A general final penetration depth equation can be given as:

$$z = K_1 \ln(1 + K_2 V^2) \qquad \textbf{2-15}$$

where K_1 and K_2 are somewhat lengthy expressions of penetrator characteristics and target properties, and are different for SCET and CCET.

And Forrestal applied the CET theory to penetration studies of different materials, such as concrete (Luk and Forrestal 1987), rock (Forrestal 1986), soil (Forrestal and Luk 1992), and metal (Forrestal, et al. 1988). Another important modification by Forrestal and his collaborators is their compressibility assumption (Forrestal and Luk 1988), in comparison to the previous incompressibility assumption, which usually over-predicts the radial stress. In 1997, Forrestal and Tzou summarized their past works, and developed a general outline for the constitutive model with compressible and incompressible materials, and elastic-plastic and elastic-cracked-plastic region response respectively. They claimed their work could be applied to different kinds of material, including concrete (Forrestal and Tzou 1997).

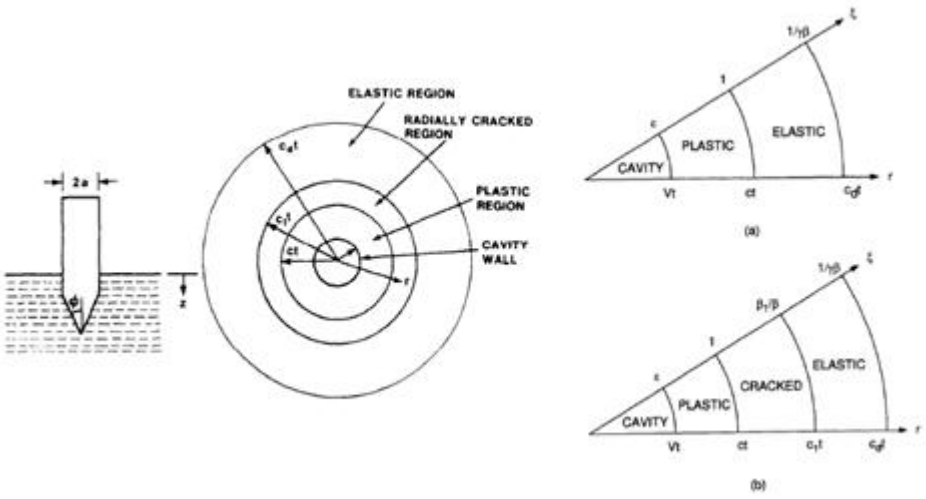

Figure 2-3. Geometry and response regions of cavity expansion theory (Forrestal 1986; Forrestal and Tzou 1997), with c, c_1- interface velocities, c_d- elastic, dilation velocity

As shown in Figure 2-3, when the projectile hits the target, a spherically symmetric cavity is expanded from zero initial radius at constant velocity V. If the V

is low enough, there are three regions of response: cracked, plastic, and elastic. As V increases, the cracked region will gradually lessen and finally diminish, leaving only the plastic and elastic regions.

Three different mechanical properties have been given to each of these three regions. For the cracked region, material is set to be linear with $\sigma_\theta = 0$; the elastic region uses Young's modulus E and Poisson's ratio v, with

$$E = 3K(1-2v) \qquad \textbf{2-16}$$

and for the plastic region, linear pressure-volumetric strain relation and Mohr-Coulomb yield criterion are adopted, with the formulae listed below:

$$p = K(1-\rho_0/\rho) = K\eta$$

$$p = (\sigma_r + \sigma_\theta + \sigma_\phi)/3; \sigma_\theta = \sigma_\phi \qquad \text{2-17}$$

$$\sigma_r - \sigma_\theta = \lambda p + \tau; \tau = [(3-\lambda)/3]Y$$

where

p- pressure; ρ_0, ρ - densities of the undeformed and deformed material; η - volumetric strain; K- bulk modulus; σ_r, σ_θ - radial and circumferential Cauchy stress; λ, τ - for pressure-dependent shear strength; Y - the uniaxial compressive strength.

Based on these given properties and mass & momentum conservation, Forrestal established the mechanical model for concrete targets with defined dimensionless parameters representing the radial stress, impact velocity, density, and compressible strength; and used the curve-fitting method for this model to show the following relationship:

$$\frac{\sigma_r}{Y} = A + B\left[\frac{V}{(Y/\rho_0)^{1/2}}\right] + C\left[\frac{V}{(Y/\rho_0)^{1/2}}\right]^2 \qquad \textbf{2-18}$$

Quasi-static response A is determined from his previous work (Forrestal and Longcope 1990), B and C are obtained from curve-fitting, shown in Table 2-1.

Table 2-1. Values of A, B, C of CET models with different assumptions (Forrestal and Tzou 1997)

Model			A	B	C
1	Incompressible	Elastic-plastic	5.18	0	3.88
2	Incompressible	Elastic-cracked-plastic	4.05	1.36	3.51
3	compressible	Elastic-plastic	4.50	0.75	1.29
4	compressible	Elastic-cracked-plastic	3.45	1.60	1.12

The final penetration depth is derived from the stress distribution integration.

$$P = \frac{m}{2\pi a^2 C N_2 \rho_0}\left\{\ln\left[1 + \frac{BN_1}{A}\left(\frac{\rho_0}{Y}\right)^{1/2} V_1 + \frac{CN_2\rho_0 V_1^2}{AY}\right] + \frac{2BN_1}{D}\left[\tan^{-1}\left(\frac{BN_1}{D}\right) - \tan^{-1}\left(\frac{CN_2(\rho_0 V^2)^{1/2}V_1 + BN_1}{D}\right)\right]\right\} \qquad \textbf{2-19}$$

where

$$D = [4ACN_2 - (BN_1)^2]^{1/2}$$

$$N_1(\psi) = \frac{(4\psi - 1)^{3/2}}{3\psi} + \frac{(2\psi - 1)^2(4\psi - 1)^{1/2}}{2\psi} - \psi(2\psi - 1)(\pi - 2\theta_0)$$

$$\theta_0 = \sin^{-1}\left(\frac{2\psi - 1}{2\psi}\right)$$

$$N_2(\psi) = \frac{8\psi - 1}{24\psi^2}$$

$$\left[\frac{m}{4\pi a^3 Y} + \frac{CN_2}{(Y/\rho_0)}\right]V_1^2 + \frac{BN_1}{(Y/\rho_0)^{1/2}}V_1 + \left[A - \frac{mV_s^2}{4\pi a^3 Y}\right] = 0$$

m - mass;

2a-shank diameter;

ψ -caliber-radius-head;

V_s -striking velocity;

As a complementary work for Luk and Forrestal on reinforced concrete (Luk and Forrestal 1987), Xu (Xu, et al. 1997) extended the spherical cavity expansion theory to include unreinforced concrete target.

$$P_t = \frac{m}{2\beta_1} \ln\left(\frac{\alpha_1 + \beta_1 V_0^2}{\alpha_1 + \beta_1 V_t^2}\right) \qquad \textbf{2-20}$$

where

$\alpha_1 = \pi a^2 p_0 A_1$ by target property

$\beta_1 = \pi a^2 p_0 B_1 \frac{8\psi - 1}{24\psi^2}$ by Projectile geometry

V_0 - impact velocity

Vt - transient velocity

Chen, X.W. (Chen and Li 2002; Li and Chen 2003) followed Forrestal's idea on ogive nose penetration, and expanded the cavity expansion theory. They proposed two dimensionless parameters N_1, N_2 relating to the nose shape and friction, and gave definitions for different nose shapes. These parameters can be incorporated to build up the force expression, along with the A and B by Forrestal (Forrestal and Luk 1988;

Luk, et al. 1991): $F_x = \frac{\pi d^2}{4}(AYN_1 + B\rho V^2 N_2)$, and integrate into a dimensionless penetration depth, with two dimensionless factors I and N.

$$\frac{X}{d} = \frac{2}{\pi} N \ln(1 + \frac{I}{N}) + \frac{k}{2} \qquad \textbf{2-21}$$

where

$$N = \frac{\lambda}{BN_2}$$

$$I = \frac{I^*}{AN_1} = \frac{MV_0^2}{d^3 YAN_1}$$

k - the crater depth

Chen and his colleagues extended their work to the oblique impact (Chen, et al. 2004) by introducing the angle of injection β into the whole derivation process.

$$\begin{cases} \frac{X}{d} = \sqrt{\frac{(4k/\pi)(1 + k\pi/4N)}{(1/I\cos^2\delta + 1/N)}} & , for \ \frac{X}{d} \le k \ or \ I\cos^2\delta \le \frac{k\pi}{4} \\ \frac{X}{d} = \frac{2}{\pi} N \ln[\frac{1 + I\cos^2\delta/N}{1 + k\pi/4N}] + k & , for \ \frac{X}{d} > k \ or \ I\cos^2\delta > \frac{k\pi}{4} \end{cases} \qquad \textbf{2-22}$$

$$\begin{cases} \delta = \sin\beta\left(1 - \sqrt{\frac{I_*}{I}}\right)^2 & , \frac{x}{d} \le k \\ \delta = \frac{k\pi}{4}\frac{\sin\beta}{I} & , \frac{x}{d} > k \end{cases}$$

2.2.3. Numerical methods

With increasing development of computer technology, people in the past 30 years have made more use of Numerical Modeling Approaches, which are usually validated by comparison with results from empirical or analytical methods.. The most common numerical modeling approaches can be grouped into three types: Finite

Elements (FE), Finite Differences (FD), Discrete Elements (DE). For the first two methods, Lagrangian and Eulerian approaches have often been applied. Heuze's summary included a table featuring the important computer programs for modeling penetration, as well as their origins, categories, and features from 1970 to 1987.

Table 2-2 is a brief program summary of numerical study on penetration research extracted from Heuze's paper. The numbers indicate the numbers of studies within each class. We grouped them specifically based on their principles, applications, and dimensions. This table can provide some information on scholars' interests in penetration computerized modeling before 1990.

Table 2-2. Summary of different methods used for penetration study before 1990

ALE – Arbitrary Langrange-Euler; CCET – Cylindrical Cavity Expansion Theory
DAFL – Differential area force law; DE – Discrete Element code
FD – Finite Difference; SCET – Spherical Cavity Expansion Theory

Theory	Number of program		
Empirical	6		
Analytical	SCET	CCET	DAFL
	2	9	4
Numerical	FE	FD	DE
	15	15	3
Dimension	1-D	2-D	3-D
	8	27	14
Structural analysis	10		
Discrete fracture	6		
Erosion	3		
ALE	6		

2.2.3.1. FEM application in penetration

FEM is a developed simulation approach. Besides the research mentioned in Heuze's summary, there are still many researchers focusing in this area after 1990, such as Warren (Warren and Tabbara 1997), using PRONTO 3D to address a practical problem; Tham, C.Y. (Tham 2006), using hydrocode to compare against empirical results; and Chen (Chen 1994) , Wang (Huang, et al. 2005) using LS-DYNA (2D);

Huang (Huang, et al. 2005), Ai-guo (Ai-guo and Feng-lei 2007) using LS-DYNA (3D). However, FEM is not of interest to this study.

2.2.3.2. DEM for penetration simulation

DEM was first introduced by Cundall in the early 1970s. It was originally applied on rocks, then extended to granular material (Cundall and Strack 1979), which triggered wider uses in different kinds of material like fluid, soil, and composites.

The basic thought of DEM is very concise: first calculate the contact force and moment of each particle based on its position and velocity through the constitutive model; secondly compute acceleration via Newton's second law, then integrate the acceleration to get the new velocity and position. The powerful calculation capability of computers makes it possible to repeat this calculation cycle billions of times in a short period until the stopping criteria is met.

DEM has not received much attention in penetration simulation before 1990. Heuze's overview (Heuze 1990) indicated that only 3 out of 33 computer programs based their theory on DEM before 1990. However, compared to other numerical simulation methods, especially those based on continuum meshing, such as FEM, DEM has its inherent advantages, especially in penetration simulation. It deals with fracturing and large deformation conveniently, allowing transition from continuum to discontinuum to be easily simulated.

Many DEM program codes have been developed or used for penetration simulation studies, including Ellipsoid (Ng 1993), TRUBAL (Tavarez and Plesha 2004), YADE, PFC3D (W-J.Shiu, et al. 2005), and BPM2D (Zhang, et al. 2005).

For projectile modeling aspect, the shape is one of the key factors affecting the penetration process. A number of studies have addressed the shapes' effect including those on flat nose (Kusano, et al. 1992; Sawamoto, et al. 1998; W-J.Shiu, et al. 2005), ogive nose (Ng 1993; Jiao, et al. 2007), and spherical ball (Magnier and Donze 1998;

Nishida, Tanaka et al. 2004). Zhang, D (Zhu and Zhang 2005) compared the shape effect on penetration using ogive and flat nose projectile. While most of researchers consider projectile as rigid, Kusano and Sawamoto (Kusano, et al. 1992; Sawamoto, et al. 1998) investigated the effects due to a deformable projectile. And about the impact velocity, Nishida (Nishida, et al. 2004) studied the penetration at a low velocity of 16m/s while others focused on velocities larger than 100m/s.

For target modeling aspect, material is the first concern for study. Researchers have used different ways to represent the material structure. For plain concrete target, Liu (Liu, et al. 2004), Nishida (Nishida, et al. 2004), Jiao (Jiao, et al. 2007) used spheres of the same size and arranged them in a close-pack pattern [Figure 2-4]. Ng (Ng 1993) used particles of randomly generated sizes [Figure 2-5]. Magnier (Magnier and Donze 1998), Sawamoto (Sawamoto, et al. 1998), Shiu (W-J.Shiu, et al. 2005) investigated the problem of penetration into reinforced concrete by incorporating steel bar represented as the lines of steel along with the concrete layer [Figure 2-6].

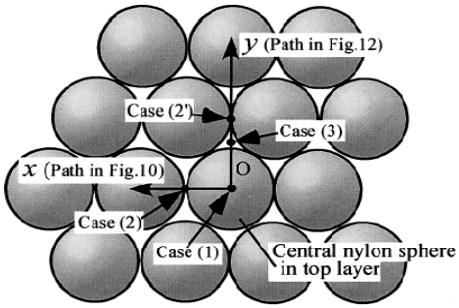

Figure 2-4. Close-pack of particles (Nishida, et al. 2004)

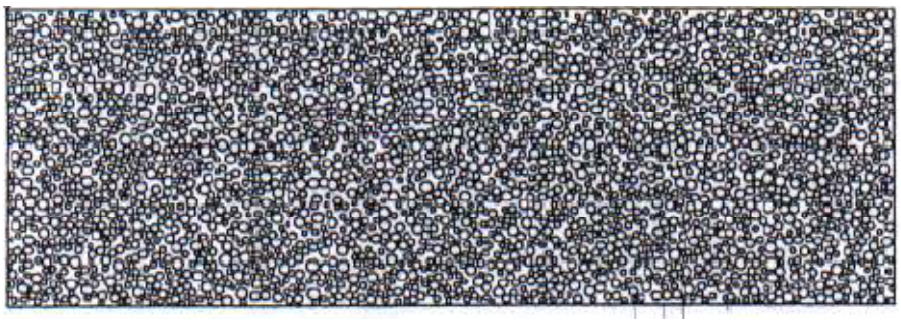

Figure 2-5. Different sizes of particles (Ng 1993)

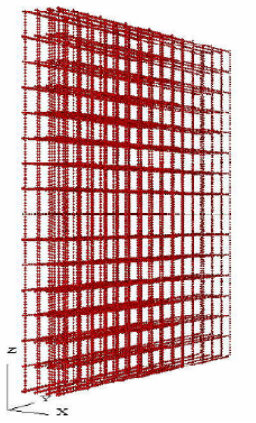

Figure 2-6. Reinforcement layer of concrete slab using DEM element (W-J.Shiu, et al. 2005)

Concerning the modeling method, Tavarez and Plesha (Tavarez and Plesha 2004) introduced the concept of cluster (bonding a number of particles) to build up a sample then compress it to the required shape. Zhu and Zhang (Zhu and Zhang 2005) made their concrete beam model by combining aggregate, represented by a cluster of elements, and sand, represented by individual elements, through the function of cement cohesion. Fu (Fu, et al. 2008) used X-ray tomography to acquire the shape of aggregates and used the cluster technique to represent complex shapes.

Besides, nearly all researchers set their target as a finite sized beam (slab or disc in 3D), different from the SI target in the empirical and analytical methods. Researchers are more concerned about the mechanics and the process of the failure of the target material, such as cratering, scabbing, tunneling, and spalling.

And due to the heterogeneous property of concrete, (i.e., not absolute axisymmetric in the 2D plane), the usage of a 3D model would be a better choice for simulation. After 2004, more effort has been spent on 3D modeling, such as Nishida, and Tanaka (Nishida, et al. 2004), Tavarez and Plesha (Tavarez and Plesha 2004), and Shiu and Donze (W-J.Shiu, et al. 2005).

Another noticeable feature is that most researchers made the comparison between simulation results and either experimental or empirical results. Liu (Liu, et al.

2004) and Zhu (Zhu and Zhang 2005) also compared their results with those obtained from other simulation methods such as FEM (LS-DYNA), while Jiao (Jiao, et al. 2007) made his comparison with Discontinuous Deformation Analysis (DDA), another discrete modeling method).

Table 2-3 summarizes several studies using DEM for simulating penetration in concrete since 1990.

Table 2-3. Key features for DEM study in penetration by different researchers since 1990

***1. Experimental, 2, Empirical, 3 Other Numerical Simulations.**

Author/ Year	Dim	Projectile			Target			Compare to
		Shape	Material	Velocity	Shape	Material	Element	
Kusano /1992	2D	cylindrical	rigid/ deformable	100,200 m/s	slab	RC	concrete	1,2*
Ng /1993	2D	ogive	Steel	328.9 m/s	slab	C	Concrete (half)	1
Magnier /1998	2D	spherical	Rigid	50-450 m/s	beam	C/RC	Concrete ,steel	1,2
Sawamoto/1998	2D	flat	rigid/ deformable	215 m/s	slab	RC	Concrete steel	
Liu /2004	2D	conic	Steel	25,50,100m/s	disc	C	concrete	1,2,3
Nishida /2004	3D	spherical	Steel	<16 m/s	slab	Agg.	aggregate	1,2
Tavarez /2004	3D	conic	Rigid	0-600 m/s	beam	C	Concrete (cluster)	2
Shiu /2005	3D	flat	Rigid	102,151, 186 m/s	slab	RC	Concrete steel	1
Zhang /2005	2D	ogive, flat	Steel	400-1200 m/s	slab	C	Aggregate, sand	1,3
Jiao /2007	2D	ogive	Hard	300 m/s	slab	C	concrete	3

Chapter 3. Methodology used for this Study

3.1. PFC3D and its Fundamental theorem

PFC 3D (Particle Flow Code in 3 Dimensions) is a commercial software developed by the ITASCA company. It is a discrete code designed to model, test, and analyze the field "where the interaction of many discrete objects exhibiting large-strain and/or fracturing is required." (refer to http://www.itascacg.com/) Because of this feature, it is widely used in different material simulations, from stiff solid fracture to rapid flow. PFC3D not only offers 'Command' to create the discrete model, but also provides its built-in programming language (called FISH code) for users to develop their own models by modifying the internal variables.

3.1.1. Particle-Flow model

The theoretical formulation of PFC3D is called particle-flow model, which makes use of DEM. The basic element of the model is particles of arbitrary shapes, which occupy a finite amount of space, and displaces independent of each other. The particles are assumed rigid, while the interaction is defined using a soft contact approach, which uses a finite normal stiffness to represent the contact stiffness.

Below are the basic assumptions for particle-flow model: (Itasca Consulting Group 2005)

1. The particles are treated as rigid bodies.

2. The contacts occur over a vanishingly small area (i.e., at a point).

3. Behavior at the contacts uses a soft-contact approach wherein the rigid

particles are allowed to overlap one another at contact points.

4. The magnitude of the overlap is related to the contact force via the force-displacement law, and all overlaps are small in relation to particle sizes.

5. Bonds can exist at contacts between particles.

6. All particles are spherical. However, the clump logic supports the creation of super-particles of arbitrary shape. Each clump consists of a set of overlapping particles that acts as a rigid body with a deformable boundary.

Force-Displacement Law and Motion Law are the two primary rules to define the mechanical behavior of this model, in which the former determines force and moment from the particles' displacement, while the latter does the opposite [Figure 3-1].

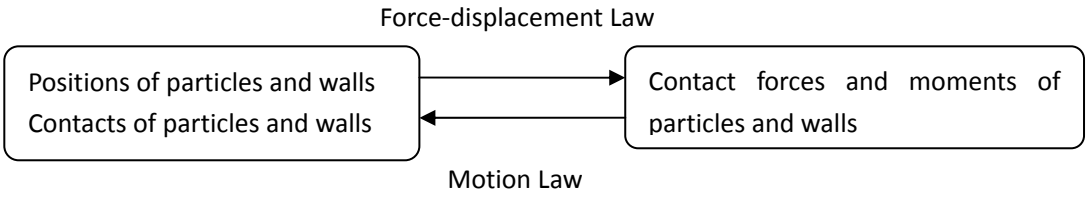

Figure 3-1. Procedure of each DEM calculation cycle

3.1.1.1. Force-Displacement Law

This Law is used to calculate the contact force and momentum between two entities based on their relative displacement. The momentum part could only be modeled in the parallel bond, described in the next section.

PFC3D uses a soft-contact approach to describe the contact force, which could be decomposed into two parts, normal and shear. $F_i = F_i^n + F_i^s$.

The overlap U^n is defined in the following equations, and illustrated in the equation and Figure 3-2.

$$U^n = \begin{cases} R^{[A]} + R^{[B]} - d(ball - ball) \\ R^{[b]} - d(ball - wall) \end{cases} \quad \textbf{3-1}$$

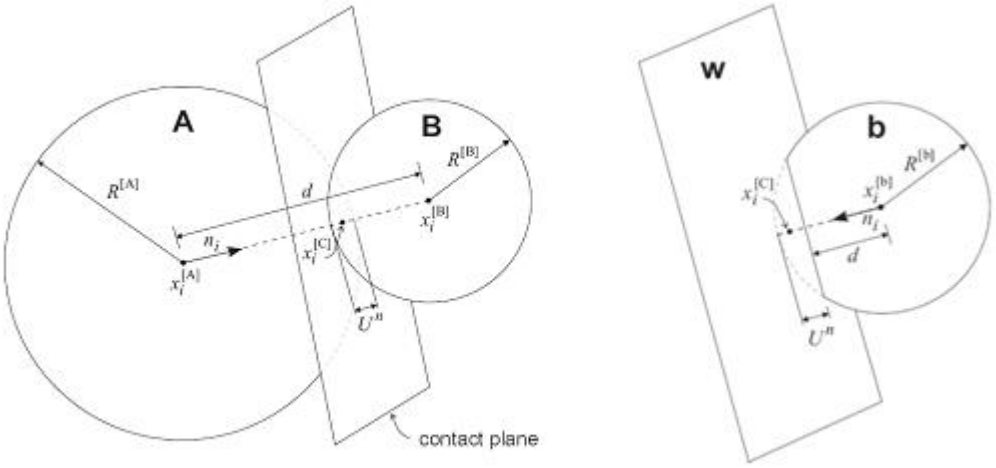

Figure 3-2. Contact stiffness model for ball-ball and ball-wall (Itasca Consulting Group 2005)

The shear force is computed in an incremental fashion, where the relative shear overlap increment ΔU_i^s is related to the contact velocity V_i^s. K^n and K^s are correspondingly the normal and shear stiffness.

3.1.1.2. Law of Motion

This law, also referred as Newton's second law, governs how force and momentum determine the particle translational and rotational motion. The equation for translational motion is $F_i = m(\ddot{x}_i - g_i)$, where *m* is the total mass of the particle; g_i is gravity of acceleration. The rotational motion is $M_i = H_i = (\frac{2}{5} mR^2)\dot{w}_i$ (simplified for the spherical particle in a global coordinate system), with R being the particle radius, M_i is the momentum, w_i the angular velocity.

3.2. Contact models applied in this study

PFC3D uses several contact constitutive models for each contact between balls

and walls to simulate the mechanical behavior in the digital material. The constitutive model of this study consists of three parts: Contact-stiffness model, Slip model, and Bonding model.

3.2.1. Contact-stiffness model (linear)

The contact-stiffness model provides an elastic relation between the contact force and relative displacement between balls and between balls and wall. The basic equations are shown below

$$F_i^n = K^n U^n n_i \quad \text{for normal forces} \tag{3-2}$$

$$\Delta F_i^s = -k^s \Delta U_i^s \quad \text{for shear forces} \tag{3-3}$$

PFC3D includes two contact-stiffness models, linear model and the simplified Hertz-Mindlin model. In this study, the linear model is used, with an assumption that the stiffness of the two contacting entities act in series. The following two variables should be designated to set up the model.

$$K^n = \frac{k_n^{[A]} k_n^{[B]}}{k_n^{[A]} + k_n^{[B]}} \quad \text{for normal stiffness} \tag{3-4}$$

$$k^s = \frac{k_s^{[A]} k_s^{[B]}}{k_s^{[A]} + k_s^{[B]}} \quad \text{for shear stiffness} \tag{3-5}$$

Where [A] and [B] denote the two entities in contact

3.2.2. Slip model

The key parameter of slip model is a dimensionless friction coefficient μ, which is the minimum of the two contacting entities. The slip occurs when $\left|F_i^s\right| > F_{\max}{}^s = \mu \left|F_i^n\right|$, then $\left|F_i^s\right| = F_{\max}{}^s$.

This slip model only coexists with parallel-bond model, which depicts the

constitutive behavior for cementatious material between entities of corresponding condition.

3.2.3. Bonding model (parallel)

Bonding model is another key model in PFC3D. It is only formed between proximate particles (not between balls and walls), and continues to exist until broken, which happens when its strengths are exceeded.

PFC3D 3.0 supports two bonding models: contact-bond model and parallel-bond model. In order to simulate cementatious function in concrete, the parallel model is used in this study.

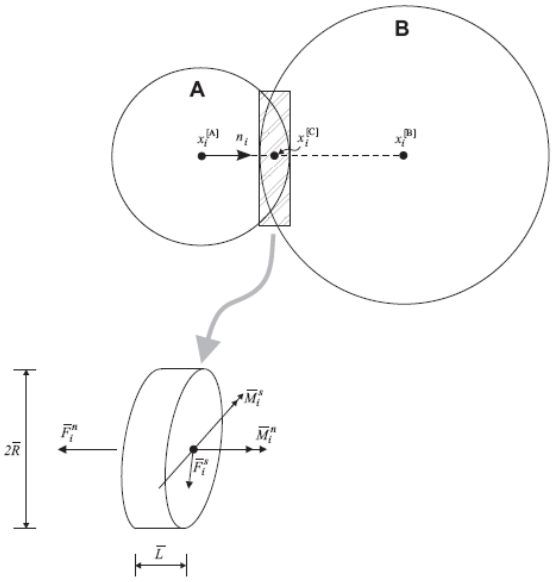

Figure 3-3. Schematic of parallel bond (Itasca Consulting Group 2005).

The Parallel bond acts over a circular cross-section as shown [Figure 3-3], which enables it to transmit both a force and a moment. Another important feature of parallel-bond is that it can act in parallel with slip model or contact-stiffness. Below are the equations governing the normal and shear components for both the force and moment: $\overline{F}_i = \overline{F}_i^{\,n} + \overline{F}_i^{\,s}$ and $\overline{M}_i = \overline{M}_i^{\,n} + \overline{M}_i^{\,s}$.

The elastic properties and the limit of the bond can be set up by designating the following factors: normal stiffness $\bar{k}^n$, shear stiffness $\bar{k}^s$; normal strength $\bar{\sigma}_c$, shear strength $\bar{\tau}_c$; and bond disk radius $\bar{R}$. The equations of defining the above variables are listed in Table 3-1.

Table 3-1. Equations of force and moment for parallel bond and corresponding parameters

Force	Normal	$\Delta\bar{F}_i^{\,n} = (-\bar{k}^n A \Delta U^n) n_i$	$\Delta U_i = V_i \Delta t$
	Shear	$\Delta\bar{F}_i^{\,s} = -\bar{k}^s A \Delta U_i^s$	
Moment	Normal	$\Delta\bar{M}_i^{\,n} = (-\bar{k}^s J \Delta\theta^n) n_i$	$\Delta\theta_i = (w_i^{[B]} - w_i^{[A]})\Delta t$
	Shear	$\Delta\bar{M}_i^{\,s} = -\bar{k}^n I \Delta\theta_i^s$	
Bond disk		$A = \pi \bar{R}^2$	
Polar moment of inertia of the disk cross-section		$J = \frac{1}{2}\pi \bar{R}^4$	
Moment of inertia of the disk cross-section		$I = \frac{1}{4}\pi \bar{R}^4$	

The maximum tensile and shear stresses of the bond periphery are calculated below to compare with the strengths; if exceeded, the bond would break.

$$\sigma_{\max} = \frac{-\bar{F}^n}{A} + \frac{\left|\bar{M}_i^{\,s}\right|}{I}\bar{R}, \quad \tau_{\max} = \frac{\left|\bar{F}_i^{\,s}\right|}{A} + \frac{\left|\bar{M}^n\right|}{I}\bar{R} \qquad 3\text{-}6$$

Table 3-2 summarizes the key factors and corresponding variables in all the constitutive models of this study, and the Figure 3-4 describes the special existing conditions for those models. It is noticed that the contact-stiffness model always exists; the slip model would change from a normal-force-related status to the maximum force status as the shear force increases; and the parallel-bond model would break when either of the normal or shear force reaches its strength valve.

Table 3-2. Key variables in different contact constitutive models in PFC3D

Model	Key Factors	Controlling variables in PFC3D
Contact-stiffness model (Linear)	Normal stiffness	md_kn
	Shear stiffness	md_ks
Slip model	Friction factor	md_fric
Bonding model (Parallel)	Normal stiffness	pb_kn
	Shear stiffness	pb_ks
	Normal strength	pb_sn
	Shear strength	pb_ss
	Radius	pb_radmult

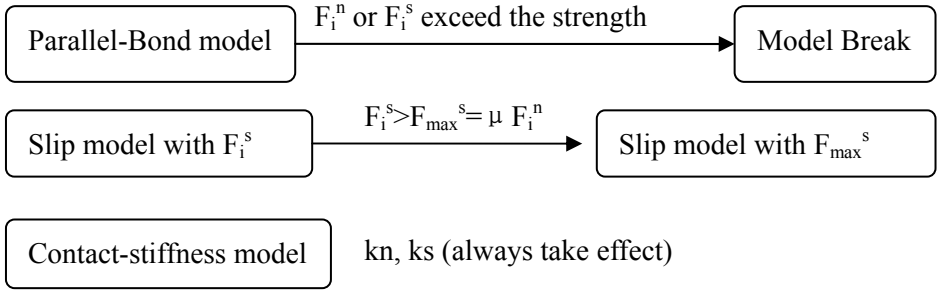

Figure 3-4. Existing condition of different contact models in DEM of PFC3D

Compared to complicated continuum models, the discrete models have fewer variables. As the material microstructure is typically computer generated, calibration is usually needed to relate these microscopic variables to the macroscopic parameters such as the elasticity modulus, Poisson's ratio, and compressive strength..

3.3. Parameters Definition and Inputs

As mentioned in previous chapter, there are several important parameters for both projectile and target, contributing to the entire penetration process significantly. In this study, some major factors for DEM modeling were selected.

For projectile, projectile mass (m), projectile diameter (dia), nose shape, and impact velocity (vel) are the four major parameters. The former three are set in the

projectile geometric and mechanical property file, while the last one is input in the main code for penetration simulation.

For target, Young's modulus (E), Poisson's ratio (ν), and Compressive strength (σ_c) are the three major parameters. Together they represent the mechanical characteristics of the material. All of them are obtained by the digital calibration uniaxial test. In order to achieve the same property of real material, the trial and error technique is used to back-calculate the micro-variables of the DEM models. The calibration process and results are explained in the later sections.

3.4. Digital Model Creation for Projectile and Target

3.4.1. Projectile Model

Mono-size balls are used for the projectile tail. The ball sizes are decreased from the junction of tail to tip to build the required cone shape. The overlap of balls and large stiffness are assigned on purpose here in order to keep a compact status inside the projectile. The clump function of PFC3D is used here to clump the balls in the projectile into one object, which allows no relative movements for all projectile balls. The friction between projectile and the target varies with their relative velocity. It is determined according to equation $f = f_{\inf} + (f_{stat} - f_{\inf})e^{-\gamma * vel}$ by (Chen 1989), in which f_{inf} is the friction with idealized infinite velocity and f_{stat} is the static friction. Figure 3-5 and Table 3-3 are the geometric and mechanical setting of an example projectile (Forrestal, et al. 1994). Table 3-4, Table 3-5, and Figure 3-6 are the corresponding DEM model setting of that projectile.

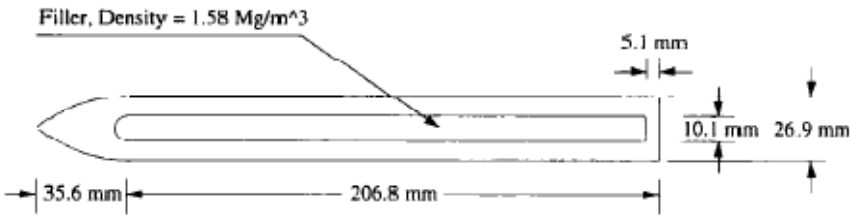

Figure 3-5. The geometry of projectile used in test (Forrestal, et al. 1994)

Table 3-3. Material properties for both projectile and the target (Forrestal, et al. 1994)

TABLE 1. PENETRATION PARAMETERS

f_c' (MPa)	13.5	13.5	36.2	96.7
ρ (kg/m^3)	1960	1960	2370	2340
m (kg)	0.0642	0.0642	0.906	0.904
$2a$ (mm)	12.7	12.7	26.9	26.9
ψ	3	4.25	2.0	2.0
N	0.106	0.076	0.156	0.156
S	21	21	12	7

Table 3-4. Example of micro-variables in digital projectile

Micro-variable	Variable in PFC3D	Value	Unit
Particle Radius	radius	7e-3	m
Density	dens_b1	2450	kg/m^3
Normal stiffness	kn_b1	150e9	Pa
Shear stiffness	ks_b1	150e9	Pa
Friction	fric_infspd	0.03	N
	fric_static	0.2	N
	gama	0.2	

Table 3-5. Corresponding macro-parameters for digital projectile

Parameter	Variable in PFC3D	Value	Unit
Length of the cone	Len_cone	3.75e-2	m
Length of the tail	Len_tail	2.03e-1	m
Length of the projectile	Len	2.40e-1	m
Diameter of the tail	Diameter	7e-3	m
Volume of the projectile	Volume	3.70e-5	m^3
Mass of the projectile	Mass	9.06e-1	kg

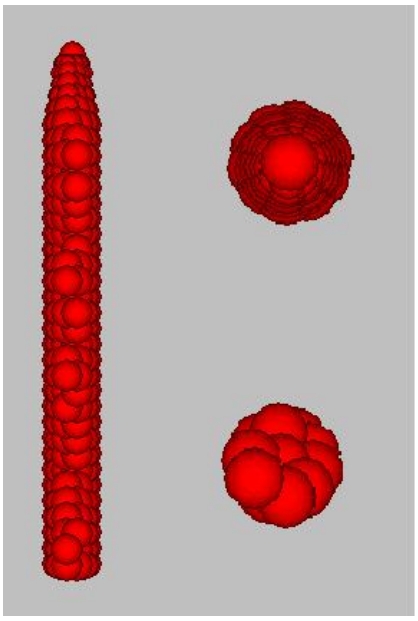

Figure 3-6. Projectile model created in DEM

3.4.2. Target Model

In experiments, cylindrical shape is usually used, which enables the convenient monitoring of symmetric damage. However, in simulatsion cubic specimen has advantages due to its simple geometry. The corner or boundary effects can be minimized through using a large dimension. Although in the classic penetration theory semi-infinite target is used, only a finite size can be used for DEM simulation. However its specific dimension needs to be determined to ensure that the size effect is not significant.

The computational time increases with the decrease of the ball radius and the decrease of the radius ratio between the largest and smallest ball. This is because either change would increase the number of balls significantly. Thus, the ball size of target is chosen based on the computing capacity of the available computer. In this study, the PFC3D is running on a DELL desktop with Intel® Core ™ 2 Duo E6750 @ 2.66GHz of CPU, and 1.96GB of RAM.

The microscopic material variables are difficult to determine. The Table 3-6，

Table 3-7 present a set of these variables, and their corresponding macro-parameters. The corresponding digital model is shown in Figure 3-7. Details on how to determine the parameters are presented in the next section on calibration of the microscopic model.

Table 3-6. Example of micro-variables in concrete target creation

Parameter		Variable in PFC3D	Value	Unit
Dimension along x-axis	xlen	et3_xlen	200e-3	m
Dimension along y-axis	ylen	et3_ylen	200e-3	m
Dimension along z-axis	zlen	et3_zlen	600e-3	m
Radius of the smallest ball		et3_rlo	5e-3	m
Ratio between radius of largest particle over smallest particle		et3_radius_ratio	2	
Radius of parallel bond between particles		pb_radmult	1	
Density		md_dens	2500	kg/m^3
Elastic modulus of contact	E_c	md_Ec	0.3e9	Pa
Ratio of normal to shear stiffness of particles	k^n / k^s	md_knoverks	1	
Elastic modulus of parallel bond	$\overline{E}_c$	pd_Ec	70e9	Pa
Ratio of normal to shear stiffness of parallel bond	$\overline{k}^n / \overline{k}^s$	pd_knoverks	3	
Particle friction coefficient	μ	md_fric	0.5	
Normal strength of parallel bond	$\overline{\sigma}_c$	pb_sn_mean	25e6	Pa
		pb_sn_sdev	0	
Shear strength of parallel bond	$\overline{\tau}_c$	pb_ss_mean	50e6	Pa
		pb_ss_sdev	0	

Table 3-7. Corresponding macro-parameters for digital concrete target

Parameter	Variable in PFC3D	Value	Unit
Young's modulus	E	28.3e9	Pa
Poisson's ratio	ν	0.18	
Compressive strength	σ_c	17.1e6	Pa

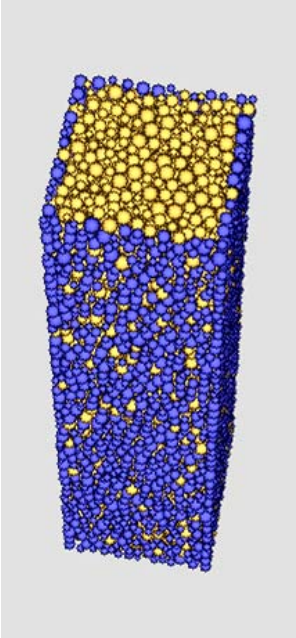

Figure 3-7. Model concrete target (The outer side of target particles are set fixed as the boundary, in color blue to simulate the fixation of real test)

The target-genesis procedure is invoked by calling PFC3D's driver et3_prep, which is included in Augmented FishTank function. In order to create a parallel-bond sample, there are four basic steps as below.

1. Initial assembly compaction. All the particles, with half of their final size are created with GENERATE command (to ensure success of generation) and placed randomly such that no two particles overlap. Final maximum radii of balls are then reached, while the whole system is allowed to get static equilibrium under zero friction, with nearly uniform force distribution, which is carried out by the et3_isopack function.

2. Big local locked-in stress would be created after the first ball generation step, and it is the second step, isotropic stress convergence, to solve this problem. A relative low stress value (compared to uniaxial compressive strength) is set at the beginning through et3_isostr, then the isotropic stress will evolve to achieve this specified value. A detailed algorithm can be

found in the manual.

3. The third step is to reduce the ‘floating’ particles, defined as those having less than three contacts with other balls. Its purpose is to obtain a denser network of bonds. The detailed process is described in the manual (Itasca Consulting Group 2005), where flt_eliminate works as the function.

4. The contact bonds installation is the last step after the above procedure. Md_add_pbonds is the function to add the parallel bond between particles in physical contact (in near proximity). Friction coefficient is then assigned to all the particles.

Chapter 4. Calibration of micro-variables in Digital Concrete and Sensitivity Analysis

4.1. Theories for the Calibration Test simulation

Uniaxial test is a test used to get the some basic mechanical properties, including Young's Modulus, Poisson's ratio, compressive strength, etc, mainly for solid material, like concrete. Figure 4-1 is a uniaxial test sketch.

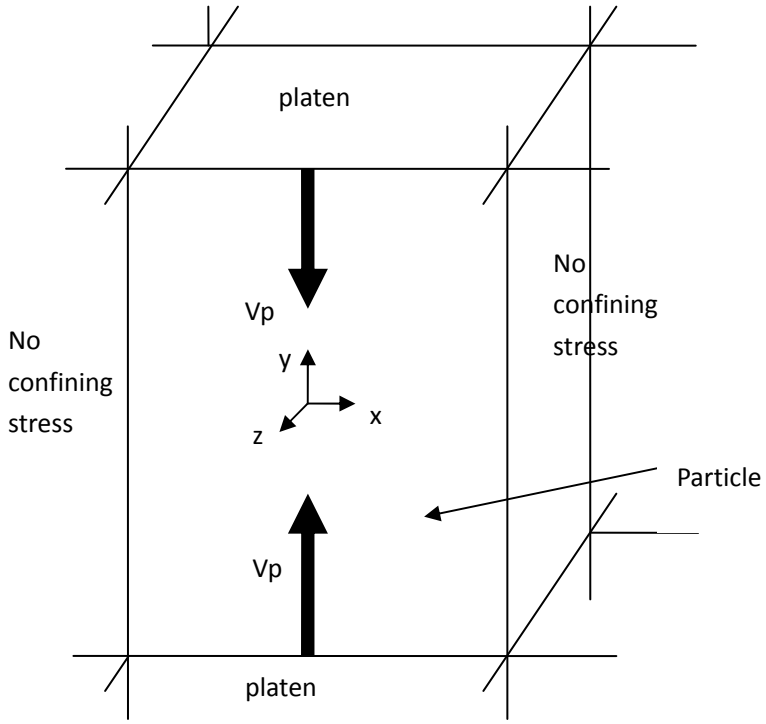

Figure 4-1. Uniaxial tests display

The simulated Uniaxial Test can be considered as a modification of Triaxial Test. The difference is that it removes the confining pressure from the surrounding walls, which is needed for unbound material (not necessary for concrete). More details can be found in the script _ttc.DVR of 'et3' drivers coding folder and PFC Manual (Itasca Consulting Group 2005).

After creating a cubic sample, A velocity v_p is applied to the top and bottom walls to simulate the loading, with inertial forces controlled, until it reaches the maximum strength limit, which corresponds to the damage of the specimen. Figure 4-2 presents the axial stress vs strain and lateral strain relationship from a simulated uniaxial test. The Young's modulus, Poisson's ratio, and Compressive strength can be obtained from it.

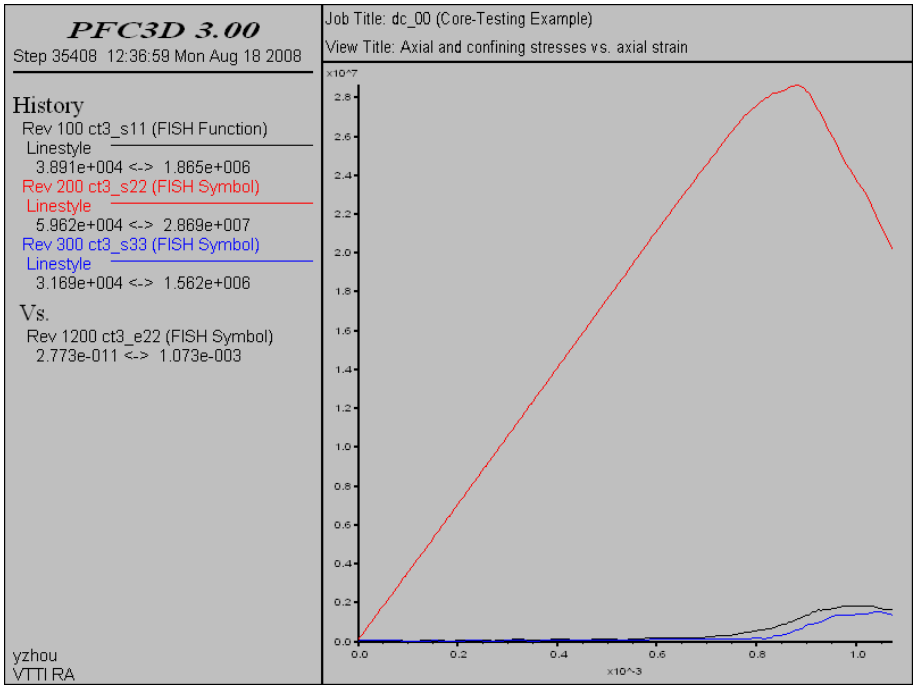

Figure 4-2. Relation between axial stress, confining stress and axial strain in uniaxial test

Table 4-1 is a summary of the macro-parameters, their major contributing micro-variables, and the corresponding simulation test to calibrate them.

Table 4-1. Macro-parameters for concrete and the corresponding major micro-variables

Macro-parameter		Major contributing micro-variables	Required test
Young's modulus	E	E_c and $\overline{E}_c$ (pb_Ec)	Uniaxial Test
Poisson's ratio	ν (or Nu)	k_n / k_s and $\overline{k}_n / \overline{k}_s$ (pb_kn/ks)	
compressive strength	σ_c (or sigc)	$\overline{\sigma}_c$ (or sn), $\overline{\tau}_c$ (or ss)(pb_kn/ks)	

4.2. Individual Effect of major Micro-variables

With the Uniaxial Test, calibration could be implemented in the simulation. However, the relationships between different micro-variables and macro-parameters are complex and have coupled influence. Thus, a trial-error method to back-calculate the micro-variables is used in this study.

An optimized calibration sequence is suggested in PFC3D for some major controlling variables in order to minimize the iterations. (mainly for parallel bond in this study).

1. Varying E_c and $\overline{E}_c$ to match the material's Young's modulus

2. Varying k_n / k_s and $\overline{k}_n / \overline{k}_s$ to match the Poisson's ratio

3. Varying the mean normal and shear strength, $\overline{\sigma}_c$ and $\overline{\tau}_c$, as well as their standard deviation, to obtain the strength envelope for both compression and tension.

4. Other properties, like post-peak behavior, crack-initiation stress and etc, can also be obtained by adjusting related variables, like friction coefficient μ to match with those from the real samples, however, they are not presented in this thesis for conciseness purpose.

4.2.1. Calibration of microscopic elastic modulus

For contact-stiffness model and parallel bond model, they have their own elastic modulus Ec and pb_Ec respectively, which contribute to the macroscopic Young's modulus. In the study three calibration tests were carried out in Table 4-2: varying Ec, varying pb_Ec, and varying both with a constant ratio.

Table 4-2. Calibration of micro-elastic modulus (contact-stiffness and parallel-bond modulus)

Micro								Macro		
E_c	$\overline{E}_c$	$E_c / \overline{E}_c$	k_n / k_s	$\overline{k}_n / \overline{k}_s$	$\overline{\sigma}_c$	$\overline{\tau}_c$	$\overline{\sigma}_c / \overline{\tau}_c$	E	ν	σ_c
GPa	GPa				MPa	MPa		Pa		Pa
With E_c varying, $\overline{E}_c$ constant										
5	25	0.25	1	1	12.5	25	0.5	20.5E+9	0.07	-22.6E+6
10	25	0.5	1	1	12.5	25	0.5	24.3E+9	0.10	-23.4E+6
25	25	1	1	1	12.5	25	0.5	35.2E+9	0.14	-28.6E+6
40	25	2	1	1	12.5	25	0.5	41.3E+9	0.20	-26.1E+6
80	25	4	1	1	12.5	25	0.5	60.0E+9	0.29	-29.8E+6
With $\overline{E}_c$ varying, E_c constant										
25	5	4	1	1	12.5	25	0.5	15.8E+9	0.36	-32.8E+6
25	10	2	1	1	12.5	25	0.5	21.9E+9	0.25	-31.0E+6
25	25	1	1	1	12.5	25	0.5	35.2E+9	0.14	-28.6E+6
25	40	0.5	1	1	12.5	25	0.5	46.6E+9	0.11	-26.6E+6
25	80	0.25	1	1	12.5	25	0.5	75.4E+9	0.08	-23.4E+6
With E_c and $\overline{E}_c$ varying, $E_c / \overline{E}_c$ constant										
5	5	1	1	1	12.5	25	0.5	6.9E+9	0.16	-26.3E+6
10	10	1	1	1	12.5	25	0.5	13.8E+9	0.16	-25.8E+6
25	25	1	1	1	12.5	25	0.5	35.2E+9	0.14	-28.6E+6
40	40	1	1	1	12.5	25	0.5	53.2E+9	0.16	-25.3E+6
80	80	1	1	1	12.5	25	0.5	108.3E+9	0.15	-27.2E+6

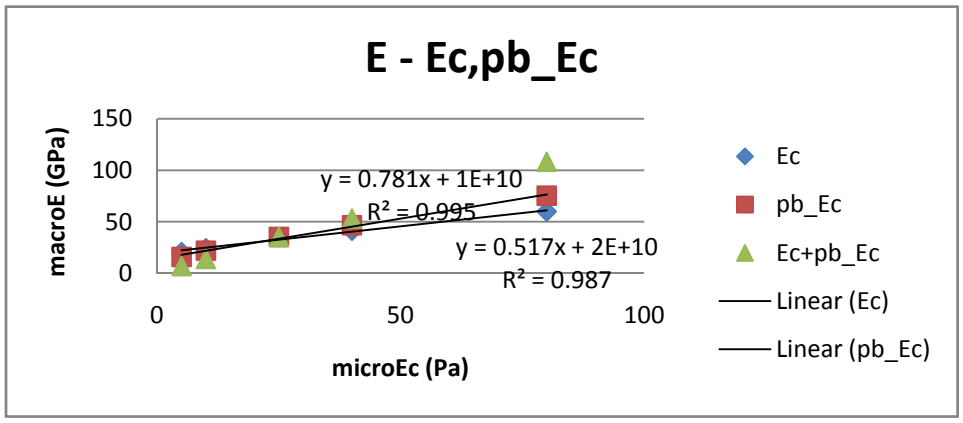

Figure 4-3. Relation between Young's modulus and micro-elastic modulus

Figure 4-3 presents the variations of macro-E from our test graphically. It can be seen that the Young's modulus of concrete increases with the increase of both Ec and pb_Ec, with the latter having a more significant influence. Another feature is that the trend for the Young's modulus over these two micro-modulus are both close to a linear relation for the range covered. The regression equations are shown with determination coefficient R^2.

$$E = 0.781E_c + 10^{10}, \text{ with } R^2=0.995 \qquad 4\text{-}1$$

$$E = 0.517\overline{E}_c + 2*10^{10}, \text{ with } R^2=0.987 \qquad 4\text{-}2$$

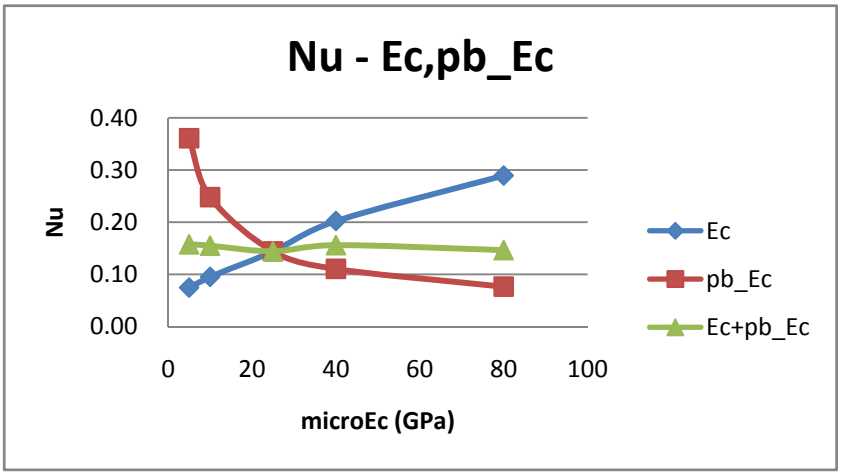

Figure 4-4. Relation between Poisson's ratio and micro-elastic modulus

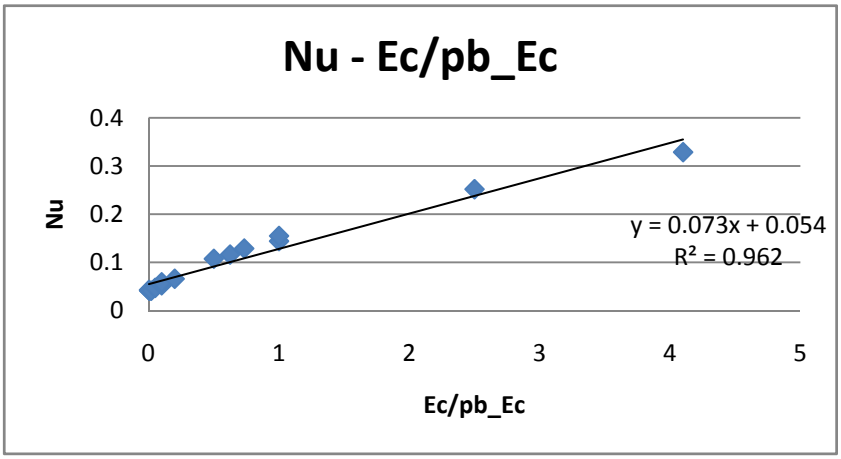

Figure 4-5. Relation between Poisson's ratio and micro-elastic modulus ratio

Figure 4-4 and Figure 4-5 show that Poisson's ratio has much more complex relations with Ec and pb_Ec. Poisson's ratio generally increases with the increase of Ec and decrease of pb_Ec, while the combining effect of both would keep it stable. And Poisson's ratio has close linear relationship with ratio of Ec/pb_Ec.

$$\nu = 0.073\frac{E_c}{\overline{E}_c} + 0.054 \text{ , with } R^2=0.962 \qquad 4\text{-}3$$

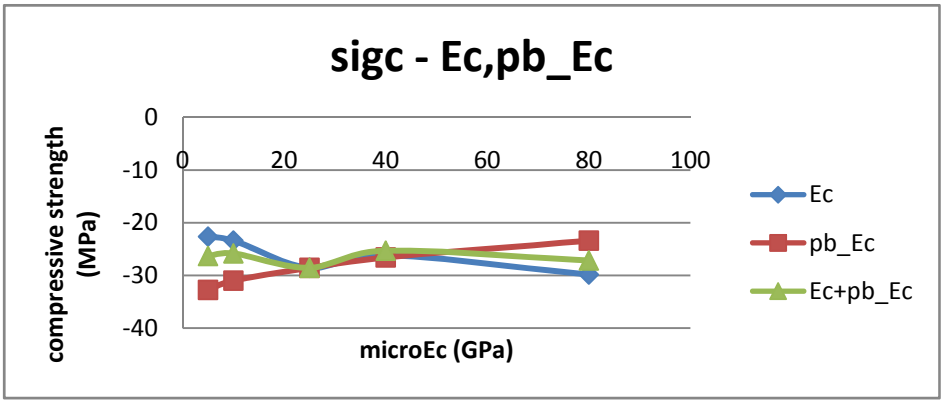

Figure 4-6. Relation between Compressive strength and micro-elastic modulus

Figure 4-6 shows that Compressive strength decreases with the pb_Ec, but has a wavy relation with Ec. And superposition can also be adopted on sigc. What should be pointed out is that the variation range of Poisson's ratio and Compressive strength, especially the latter, don't have too much dependence on Ec and pb_Ec. They depend more on the other variables explained afterwards.

4.2.2. Calibration of microscopic normal over shear stiffness ratio

For contact-stiffness model and parallel bond model, they have their own ratio of normal over shear stiffness kn/ks and pb_kn/ks respectively. These are the two major micro-variables contributing to Poisson's ratio. Three calibration tests were carried out in Table 4-3: varying kn/ks, varying pb_kn/ks, and varying both with a constant ratio.

Table 4-3. Calibration of micro-kn/ks (contact-stiffness modulus and parallel-bond modulus)

Micro								Macro		
E_c	$\overline{E}_c$	$E_c / \overline{E}_c$	k_n / k_s	$\overline{k}_n / \overline{k}_s$	$\overline{\sigma}_c$	$\overline{\tau}_c$	$\overline{\sigma}_c / \overline{\tau}_c$	E	ν	σ_c
GPa	GPa				MPa	MPa		Pa		Pa
With E_c varying, $\overline{E}_c$ constant										
25	25	1	0.2	1	12.5	25	0.5	35.1E+9	0.16	-26.5E+6
25	25	1	0.5	1	12.5	25	0.5	34.6E+9	0.15	-26.0E+6
25	25	1	1	1	12.5	25	0.5	35.2E+9	0.14	-28.6E+6
25	25	1	2	1	12.5	25	0.5	33.3E+9	0.17	-26.6E+6
25	25	1	5	1	12.5	25	0.5	31.9E+9	0.18	-25.7E+6
With $\overline{E}_c$ varying, E_c constant										
25	25	s	1	0.2	12.5	25	0.5	60.6E+9	(0.08)	-18.0E+6
25	25	1	1	0.5	12.5	25	0.5	44.5E+9	0.05	-24.6E+6
25	25	1	1	1	12.5	25	0.5	35.2E+9	0.14	-28.6E+6
25	25	1	1	2	12.5	25	0.5	27.8E+9	0.22	-24.5E+6
25	25	1	1	5	12.5	25	0.5	20.6E+9	0.30	-18.2E+6
With E_c and $\overline{E}_c$ varying, $E_c / \overline{E}_c$ constant										
25	25	1	0.2	0.2	12.5	25	0.5	58.8E+9	(0.07)	-16.7E+6
25	25	1	0.5	0.5	12.5	25	0.5	43.3E+9	0.06	-24.1E+6
25	25	1	1	1	12.5	25	0.5	35.2E+9	0.14	-28.6E+6
25	25	1	2	2	12.5	25	0.5	26.5E+9	0.25	-22.9E+6
25	25	1	5	5	12.5	25	0.5	19.0E+9	0.32	-17.7E+6

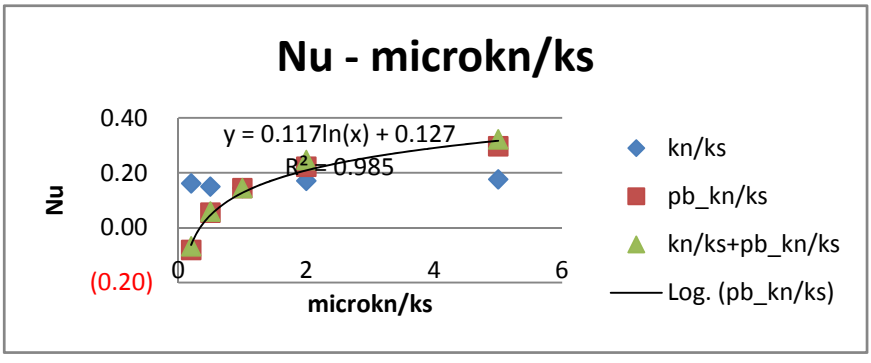

Figure 4-7. Relation between Poisson's ratio and micro-kn/ks

Figure 4-7 above presents the variation of micro-kn/ks from the test. As shown,

Poisson's ratio is more affected by the pb_kn/ks, while kn/ks has no significant effect (kn/ks varies from 0.2 to 5, but the ν changes very little). A logarithmic regression can be used to present the correlation between ν and pb_kn/ks.

$$\nu = 0.117 \ln \frac{\bar{k}_n}{\bar{k}_s} + 0.127 \text{, with } R^2=0.985 \qquad 4\text{-}4$$

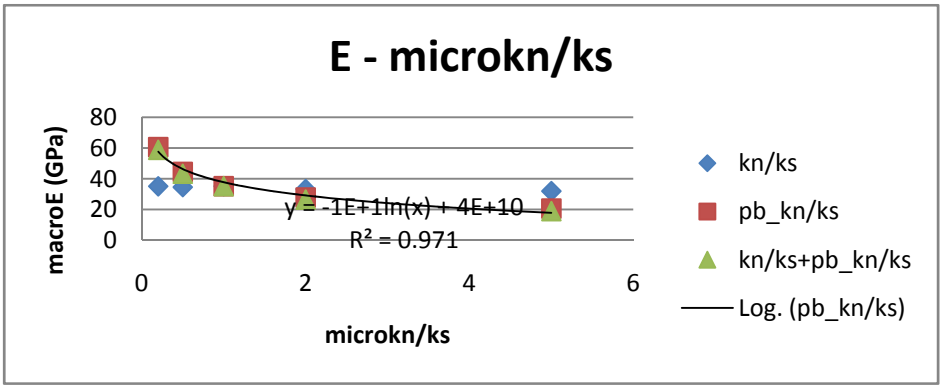

Figure 4-8. Relation between Young's modulus and micro-kn/ks

As shown in Figure 4-8, the influence on Young's modulus is similar to the case of Poisson's ratio. The macro- elastic modulus has logarithmic relationship with pb_kn/ks, while kn/ks has no significant effect on E.

$$E = -10 * \ln \frac{\bar{k}_n}{\bar{k}_s} + 4 * 10^{10} \text{, with } R^2=0.971 \qquad 4\text{-}5$$

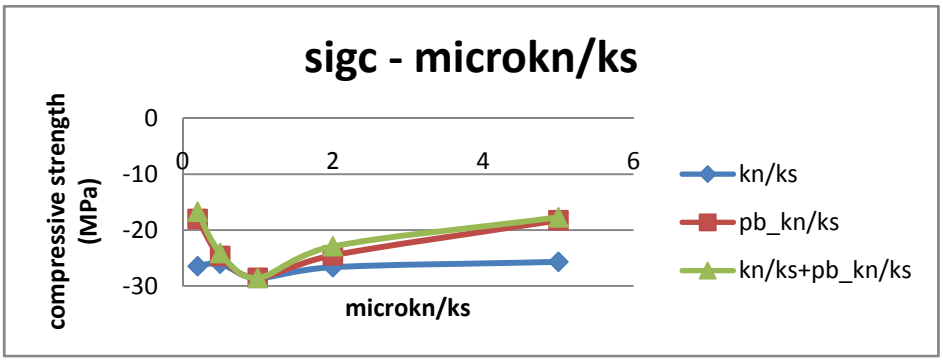

Figure 4-9. Relation between Compressive strength and micro-kn/ks

Figure 4-9 shows the effects of both ratios on Compressive strength are similar to the case of Poisson's ratio. pb_kn/ks has a bigger effect and there's an apex at kn/ks=1, pb_kn/ks=1, which makes the whole relation not monotonous.

4.2.3. Calibration of Normal and shear strength for parallel bond

Normal strength sn and shear strength ss for parallel bond are the two major micro-variables contributing to the material's Compressive strength. Three calibration tests were carried out in Table 4-4: varying sn, varying ss, and varying both with a constant ratio.

Table 4-4. Calibration of micro-strength (normal and shear strength for the particle)

Micro								Macro		
E_c	$\overline{E}_c$	$E_c / \overline{E}_c$	k_n / k_s	$\overline{k}_n / \overline{k}_s$	$\overline{\sigma}_c$	$\overline{\tau}_c$	$\overline{\sigma}_c / \overline{\tau}_c$	E	ν	σ_c
GPa	GPa				MPa	MPa		Pa		Pa
With E_c varying, $\overline{E}_c$ constant										
25	25	1	1	1	2	25	0.08	35.3E+9	0.14	-6.5E+6
25	25	1	1	1	5	25	0.2	35.2E+9	0.15	-13.9E+6
25	25	1	1	1	12.5	25	0.5	35.2E+9	0.14	-28.6E+6
25	25	1	1	1	25	25	1	35.2E+9	0.15	-33.1E+6
25	25	1	1	1	40	25	1.6	35.2E+9	0.15	-33.8E+6
With $\overline{E}_c$ varying, E_c constant										
25	25	1	1	1	12.5	5	2.5	35.3E+9	0.15	-7.3E+6
25	25	1	1	1	12.5	12.5	1	35.2E+9	0.14	-17.0E+6
25	25	1	1	1	12.5	25	0.5	35.2E+9	0.14	-28.6E+6
25	25	1	1	1	12.5	40	0.3125	35.2E+9	0.15	-32.1E+6
25	25	1	1	1	12.5	50	0.25	35.2E+9	0.15	-32.2E+6
With E_c and $\overline{E}_c$ varying, $E_c / \overline{E}_c$ constant										
25	25	1	1	1	2	4	0.5	35.5E+9	0.12	-5.1E+6
25	25	1	1	1	5	10	0.5	35.1E+9	0.15	-12.1E+6
25	25	1	1	1	12.5	25	0.5	35.2E+9	0.14	-28.6E+6
25	25	1	1	1	20	40	0.5	35.2E+9	0.15	-45.4E+6
25	25	1	1	1	25	50	0.5	35.2E+9	0.15	-57.0E+6

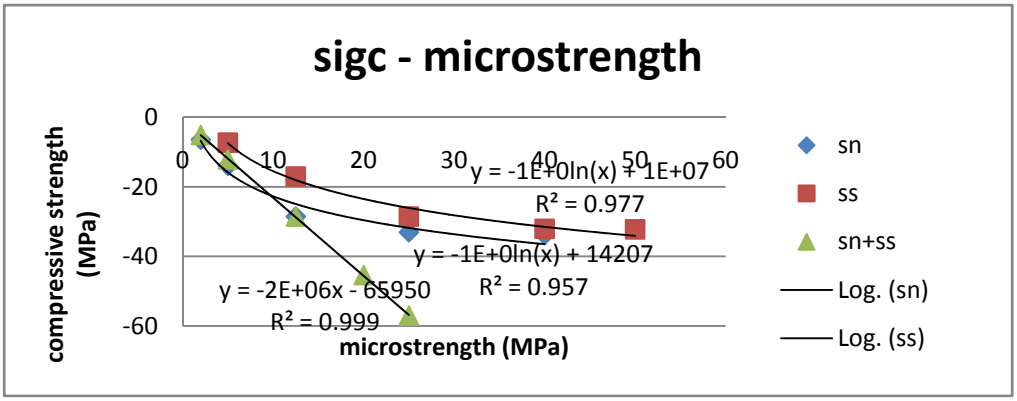

Figure 4-10. Relation between Compressive strength and micro-strength

As illustrated in Figure 4-10, the macro-Compressive strength increases with the increase of sn or ss, while sn contributes a little more. An important feature for this case is that it is the smaller one of these two micro-strengths controlling the upper limit of the macro-strength, i.e. the Compressive strength won't further increase with the large increase of one micro-strength while the other one keeps a low value. A series of tests were conducted to study the correlation between sigc and ss, sn. First, ss was changed but sn was kept the same; then sn was changed but ss was kept the same.

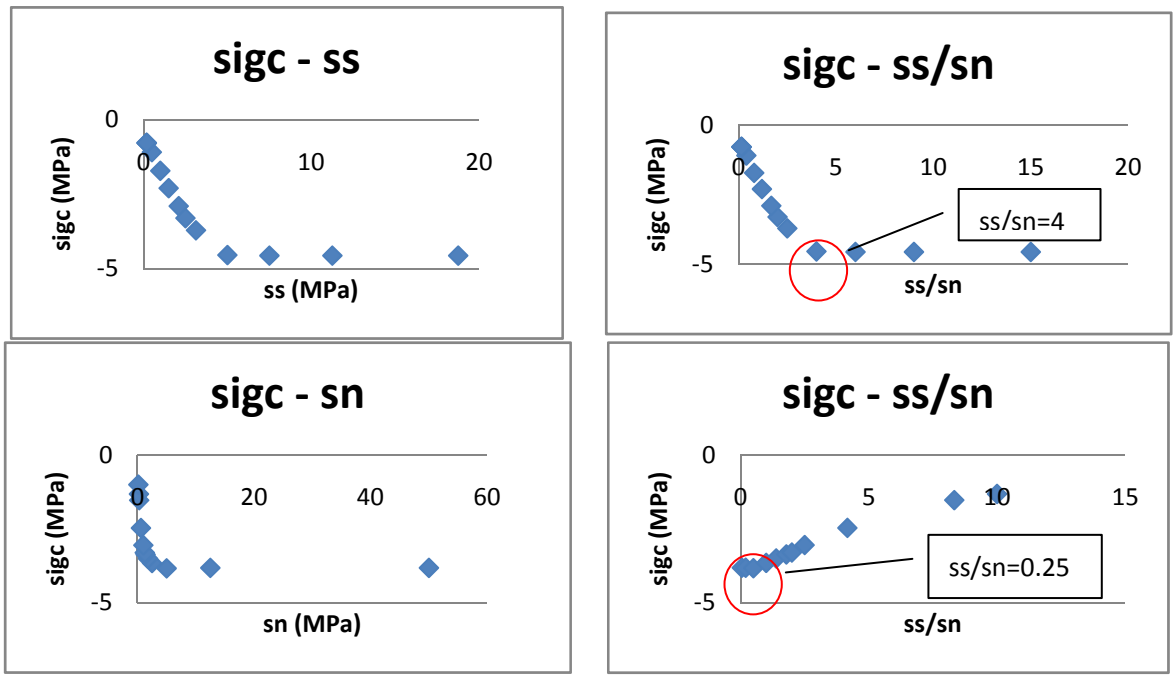

Figure 4-11. Relation between Compressive strength and micro-strength

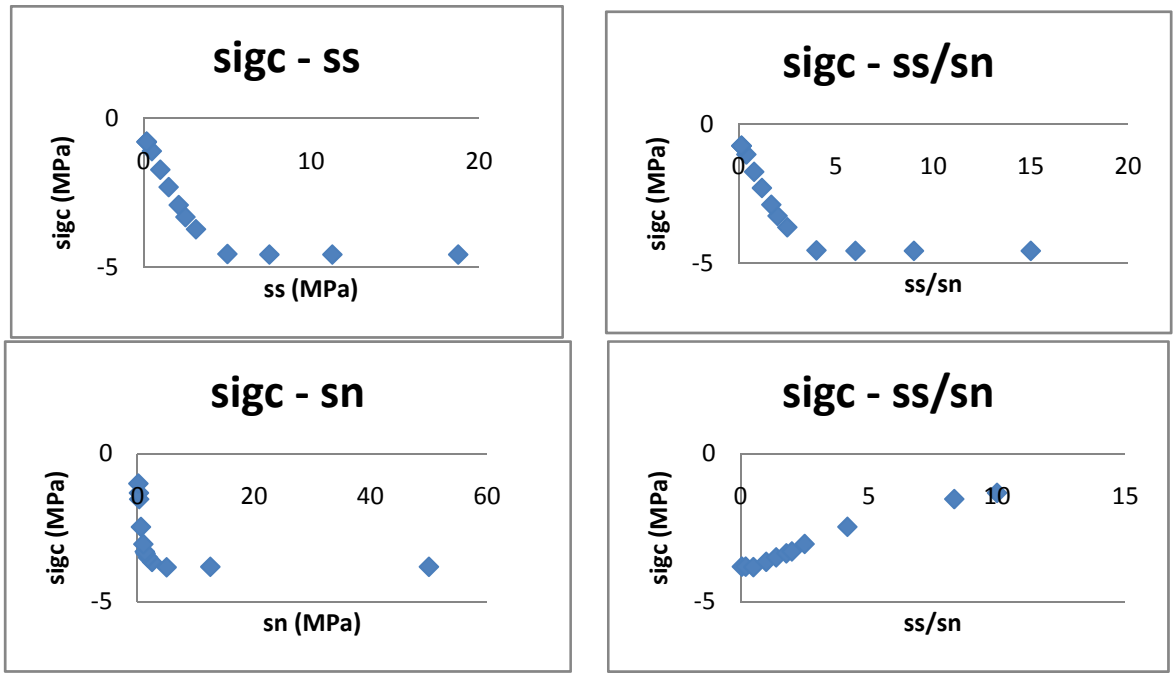

Figure 4-11 show that the relationship between the Compressive strength of the specimen and the bond strength among particles is complex. When ss is much larger than sn (ss/sn>4), sigc is mainly determined by sn, but independent of ss. When sn is much larger than sn (ss/sn<0.25), sigc is mainly determined by ss, but independent of sn. As for the range in-between (0.25<ss/sn<4), both ss and sn have effect on the sigc.

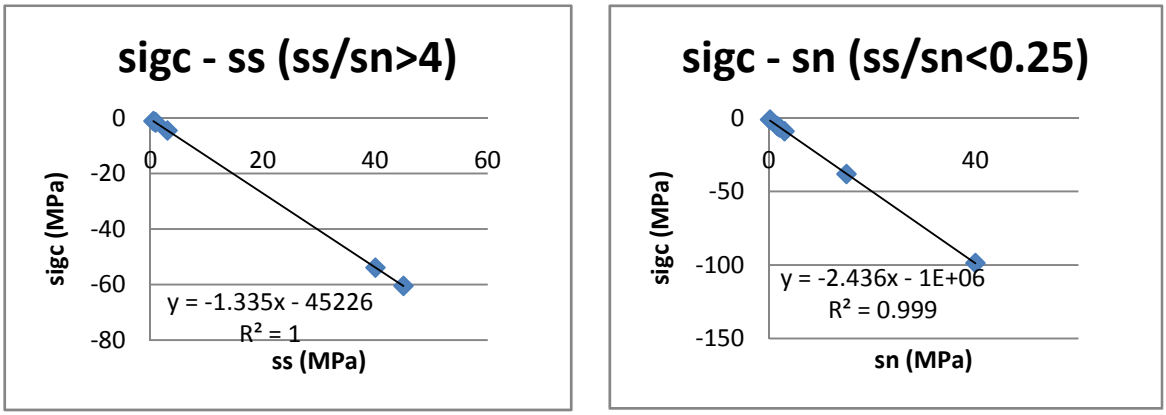

Figure 4-12. Relation between Compressive strength and micro-strength

Using the regression function of EXCEL, we can find the linear correlations for all the three cases. The first case is linear correlation between sigc and sn, the

second case is linear correlation sigc and ss, and the third case is multiple linear correlation sigc and sn, ss, as shown in Figure 4-12 and following equations.

$$\sigma_c = \begin{cases} -1.335\tau - 45226 & ,\tau/\sigma < 0.25 \quad ,with \quad R^2 = 1 \\ -0.249\sigma\text{-}0.752\tau & ,0.25 \le \tau/\sigma \le 4 \ ,with \quad R^2 = 0.984 \\ -2.436\sigma - 1e6 & ,\tau/\sigma > 4 \quad ,with \quad R^2 = 0.999 \end{cases} \qquad 4\text{-}6$$

What should be emphasized is that in the range 0.25<ss/sn<4, the regression equation is an average result. Coefficient in front of ss would increase, while coefficient in front of sn would decrease, if the ss/sn becomes closer to 0.25. And the change would reverse if the ss/sn becomes closer to 4. The integral correlation between micro-variables and macro-parameters would become more complex if other variables are taken into account.

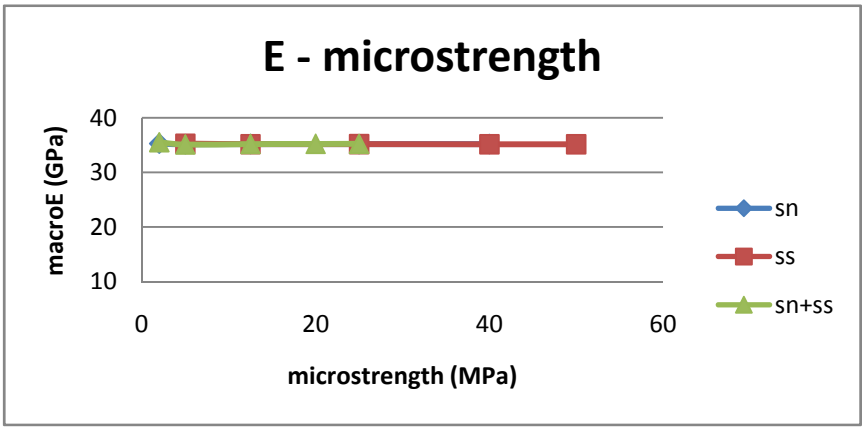

Figure 4-13. Relation between Young's modulus and micro-strength

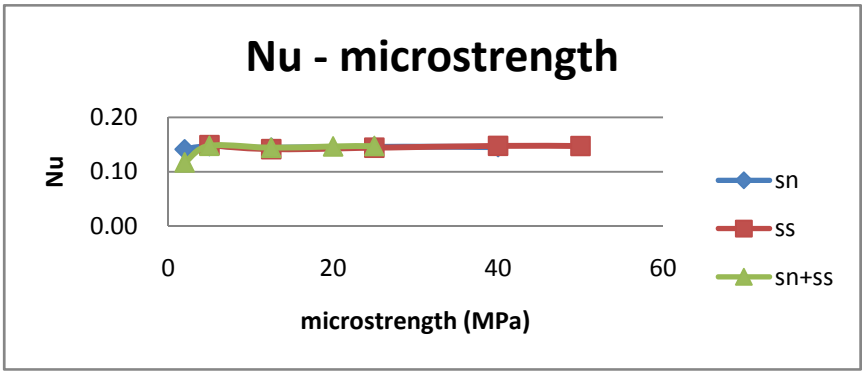

Figure 4-14. Relation between Poisson's ratio and micro-strength

For Young's modulus and Poisson's ratio, neither the sn nor ss has much contribution in the normal range. ss or sn varies from less than 5MPa to more than 50 MPa, but the modulus and Poisson's ratio change very little. Thus, it is reasonable to argue that the dependency of Elastic Modulus and Poisson's ratio on sn and ss is weak, as shown in Figure 4-13 and Figure 4-14.

4.2.4. Calibration of friction among particles

The friction factor in the concrete (not equal to the friction between penetrator and target) is another important variable which determines the sample macro-property [Table 4-5].

Table 4-5. Calibration of friction among particles

Micro							
E_c	$\overline{E}_c$	$E_c / \overline{E}_c$	k_n / k_s	$\overline{k}_n / \overline{k}_s$	$\overline{\sigma}_c$	$\overline{\tau}_c$	$\overline{\sigma}_c / \overline{\tau}_c$
GPa	GPa				MPa	MPa	
25	25	1	1	1	12.5	25	0.5
Micro			Macro				
Friction μ			E		ν		σ_c
			GPa				MPa
0			30.13503		0.210734375		-22.8406
0.1			31.17833		0.194852453		-24.276
0.2			32.24583		0.180188679		-25.3916
0.3			33.30542		0.166200818		-26.5408
0.4			34.29485		0.154138015		-27.8505
0.5			35.19068		0.144166179		-28.5577
0.6			35.97479		0.136078729		-29.3599
0.7			36.64224		0.130007224		-30.1688
0.8			37.25414		0.123512812		-29.9191
0.9			37.77215		0.118802472		-30.4271
1			38.23878		0.115083392		-30.9427

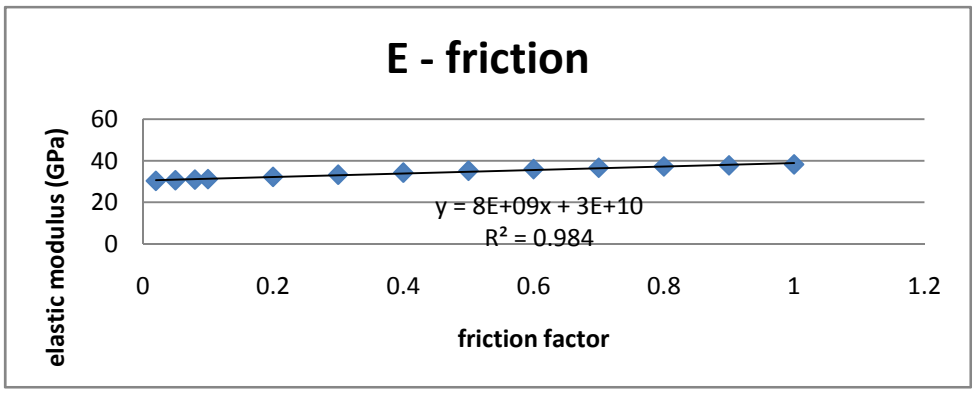

Figure 4-15. Relation between Young's modulus and friction

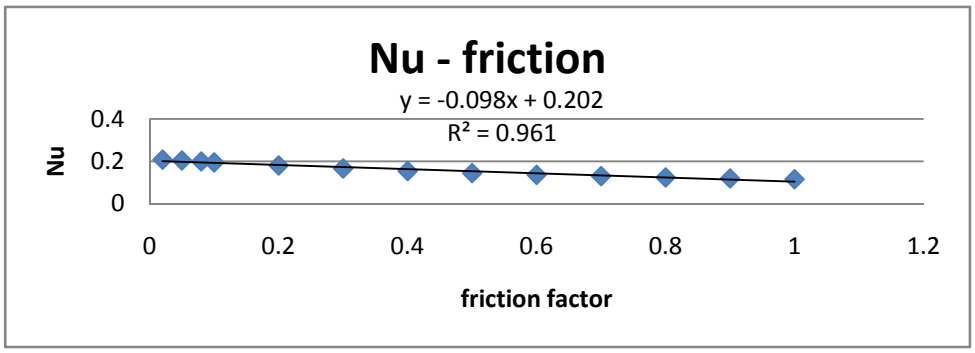

Figure 4-16. Relation between Poisson's ratio and friction

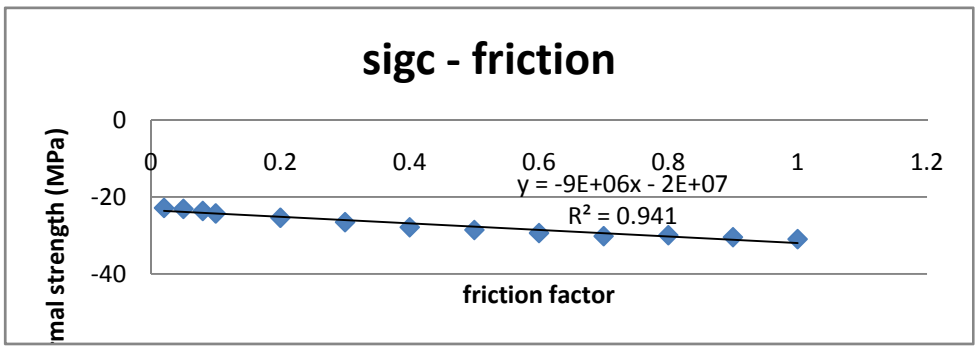

Figure 4-17. Relation between Compressive strength and friction

Varying the fric, Young's modulus, Poisson's ratio, and Compressive strength have close linear trends. The regression equations are listed in Figure 4-15, Figure 4-16, and Figure 4-17respectively. Another noticeable feature is that the variation

ranges for three macro-parameters are not large.

$$E = 8*10^{9}\mu + 3*10^{10}, \text{ with } R^2=0.995 \quad 4\text{-}7$$

$$\nu = -0.098\mu + 0.202, \text{ with } R^2=0.961 \quad 4\text{-}8$$

$$\sigma_c = -9*10^{6}\mu - 2*10^{7}, \text{ with } R^2=0.941 \quad 4\text{-}9$$

Because Uniaxial Test was conducted under quasi-static loading, we dropped out the loading velocity. Another consideration is the selection of particle size. Huang (Huang 1999) assumed its effect is too small to be taken into account in PFC2D. We applied the same assumption in PFC3D, while another major reason for this is because the decrease in particle size would largely increase the calculation time, which makes this simulation not practical for normal computer settings.

In addition to the key variables, there are other variables, like the parallel bond radius, the standard deviation of the bond strength, etc. which also affect the sample mechanical property. An extensive calibration test program series were conducted on those minor variables. However, it was found that their effects on macro-properties were either not as big as the major ones or far too irregular to do the proper analysis.

4.3. Multi-Effect Analysis and Regression Development

Based on the individual correlation between different macro-parameters and micro-variables in the last section, those micro-variables were changed simultaneously to investigate their combined effect. If some variables have interdependent effect on each other, a nonlinear part would be introduced in the regression equations.

4.3.1. Young's Modulus

As found in the last section, Young's modulus (E) has well-regulated

correlation with E_c, $\overline{E}_c$, $\overline{k}_n / \overline{k}_s$, and μ. Therein, E_c and $\overline{E}_c$ can be viewed as the direct variables affecting E, while $\overline{k}_n / \overline{k}_s$, and μ are the indirect ones.

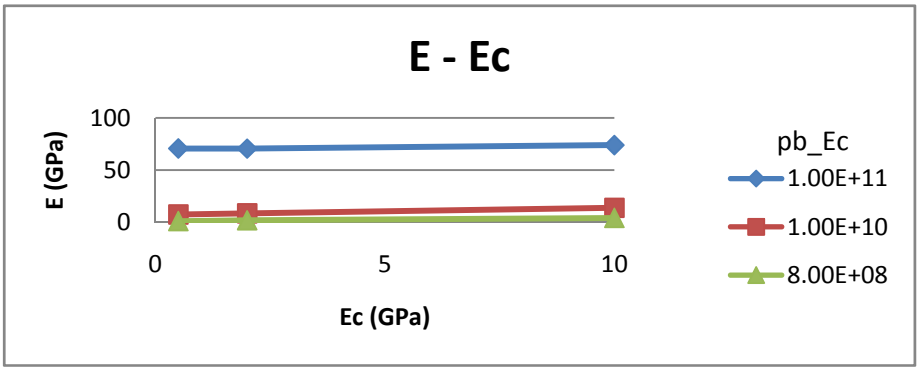

Figure 4-18. Combined effects of Ec and pb_Ec on Young's Modulus

As seen in Figure 4-18, both Ec and pb_Ec have very stable effect on E. It seems that the effects of Ec and pb_Ec on E are independent of each other. A regression format is provided below in order to keep the unit unification on both sides of the equation.

$$E = (a_E E_c + b_E \overline{E}_c)\Phi_E(\frac{\overline{k}_n}{\overline{k}_s}, \mu) \qquad 4\text{-}10$$

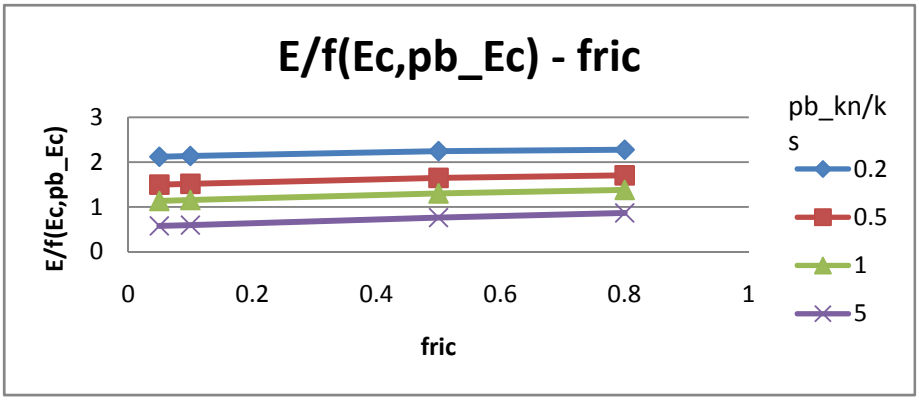

Figure 4-19. Combined effects of friction and pb_kn/ks on Young's Modulus

As seen in Figure 4-19, both pb_k_n/k_s and friction have very stable effect on E. It seems that the effects of pb_k_n/k_s and friction on E are independent of each other.

The regression equation is proposed below.

$$\frac{E}{a_E E_c + b_E \overline{E}_c} = -c_E \ln \frac{\overline{k}_n}{\overline{k}_s} + d_E \mu + e_E \qquad 4\text{-}11$$

Use 'Multi-linear' regression function of EXCEL to obtain the coefficients for different variables. The equation is listed below with the determination coefficient R^2.

$$\frac{E}{0.375E_c + 0.705\overline{E}_c} = -0.419 \ln \frac{\overline{k}_n}{\overline{k}_s} + 0.386\mu + 1.076 \text{, with } R^2=0.929 \qquad 4\text{-}12$$

4.3.2. Poisson's Ratio

As found in the last section, Poisson's ratio (ν) has well-regulated correlation with $E_c / \overline{E}_c$, $\overline{k}_n / \overline{k}_s$, and μ, in which $\overline{k}_n / \overline{k}_s$ is the major variable. A regression format is listed below for keeping the unit unification on both sides of the equation.

$$\nu = \Phi_\nu \left(\frac{E_c}{\overline{E}_c}, \frac{\overline{k}_n}{\overline{k}_s}, \mu \right) \qquad 4\text{-}13$$

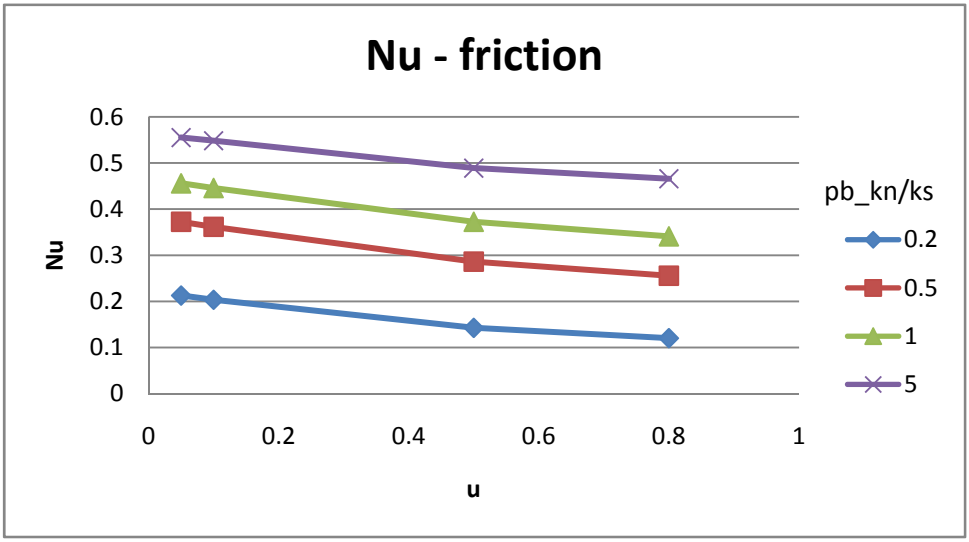

Figure 4-20. Combined effects of friction and pb_kn/ks on Poisson's ratio

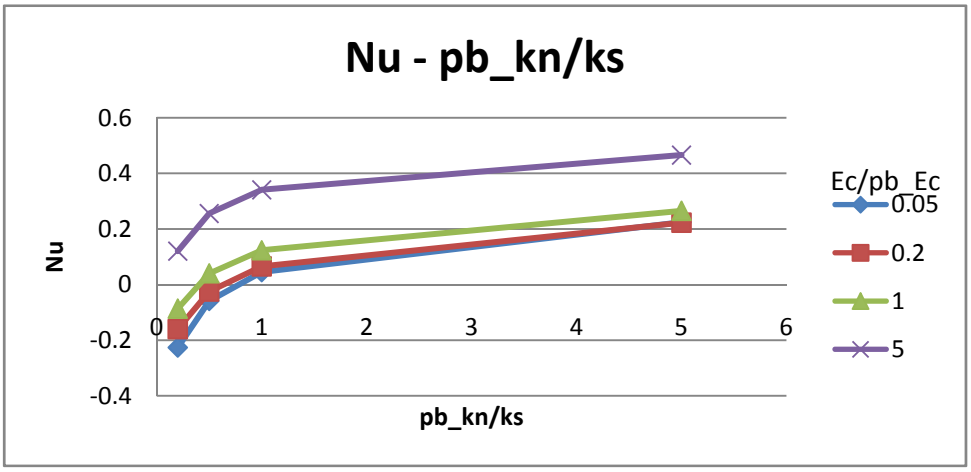

Figure 4-21. Combined effects of pb_kn/ks and Ec/pb_Ec on Poisson's ratio

As seen in Figure 4-20 and Figure 4-21, both pb_k_n/k_s and friction have very stable effects on ν . It seems that the effects of pb_k_n/k_s and friction on ν are independent of each other. The similar conclusion can be drawn for pb_k_n/k_s and E_c/pb_E_c.

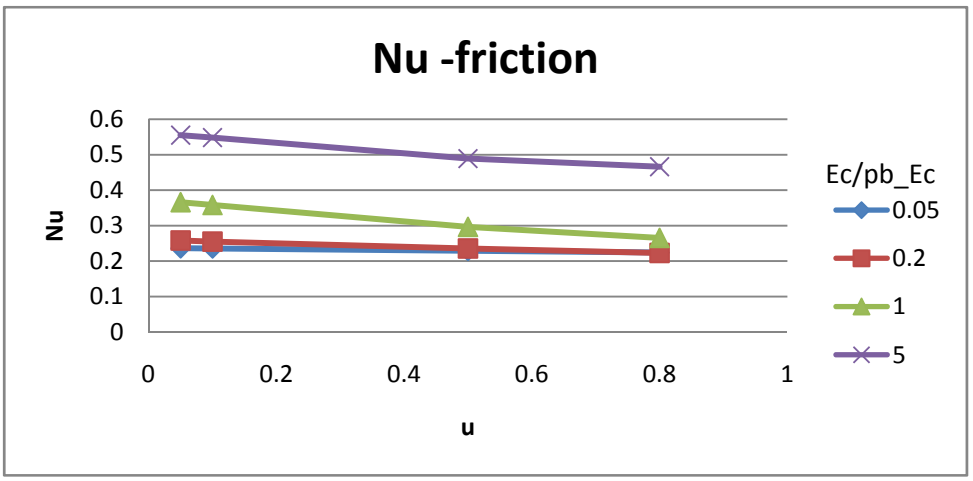

Figure 4-22. Combined effects of Ec/pb_Ec and friction on Poisson's ratio

However, for the correlation between friction and E_c/pb_E_c, a slight interdependency could be found, shown in Figure 4-22. Thus, we introduce a nonlinear term in the equation.

$$\nu = a_\nu \frac{E_c}{\overline{E}_c} + b_\nu \ln \frac{\overline{k}_n}{\overline{k}_s} + c_\nu \mu + d_\nu \frac{E_c}{\overline{E}_c} \mu + e_\nu \qquad \text{4-14}$$

The 'Multi-linear' regression function of EXCEL was used to obtain the coefficients for different variables.

$$\nu = -0.001 \frac{E_c}{\overline{E}_c} + 0.173 \ln \frac{\overline{k}_n}{\overline{k}_s} - 0.158\mu + 0.0634 \frac{E_c}{\overline{E}_c} \mu + 0.129 \text{ , with } R^2=0.958$$

4-15

4.3.3. Compressive Strength

Compressive strength (σ_c) has correlation with τ, σ, $E_c / \overline{E}_c$, $\overline{k}_n / \overline{k}_s$, and μ, in which τ and σ are the major variables, with linear relationship. A regression is provided below in order to keep unit unification on both sides of the equation.

$$\frac{\sigma_c}{\Phi_1(\tau, \sigma)} = \Phi_2\left(\frac{\overline{k}_n}{\overline{k}_s}, \mu_{,c} \frac{E_c}{\overline{E}_c}\right) \qquad \text{4-16}$$

As stated before, the discussion of sigc was divided into into three ss/sn range: <0.25, 0.25-4, >4. Series of tests were conducted to investigate the individual and combined effect of different variables in these three ranges respectively.

Table 4-6. Individual effects of micro-variables on Compressive Strength

Micro-parameter	Range of ss/sn	Graphical correlation

pb_kn/ks	<0.25	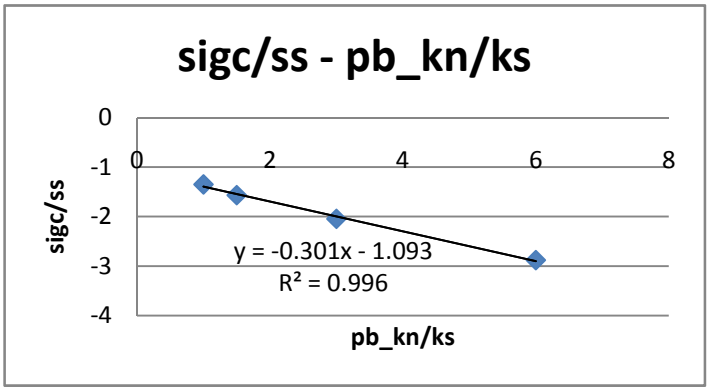
	0.25-4	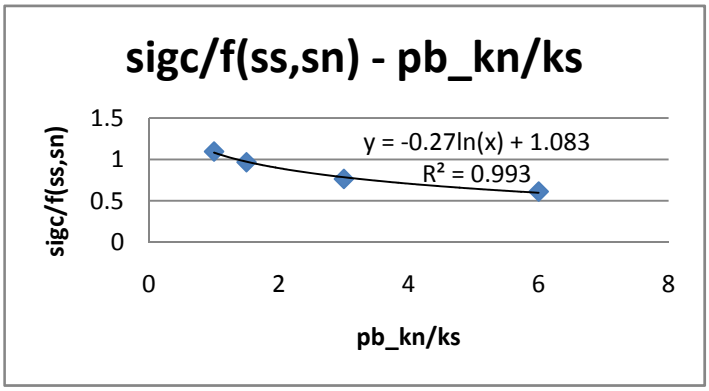
	>4	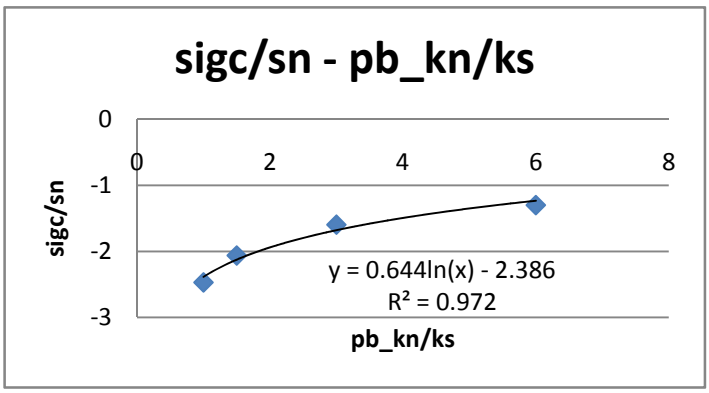
friction	<0.25	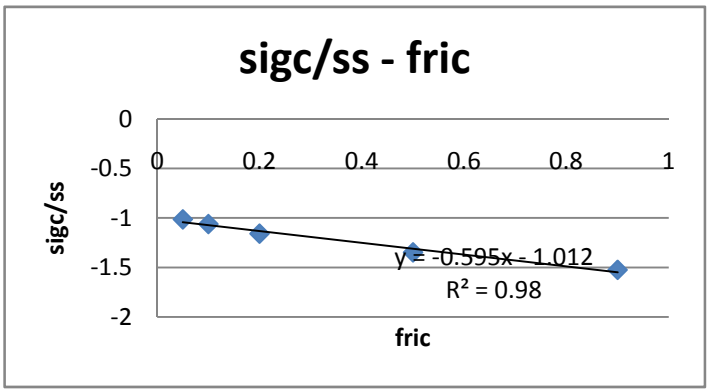

	0.25-4	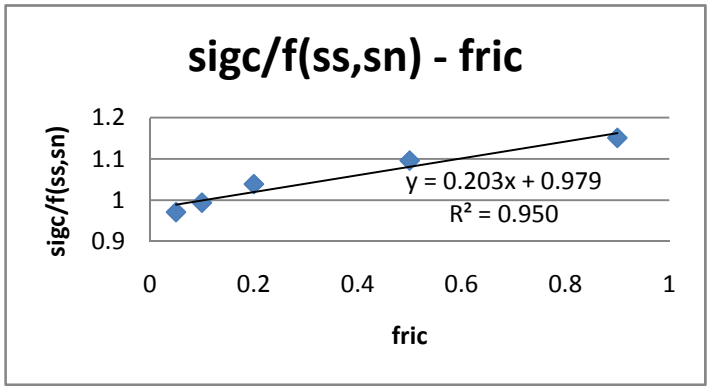
	>4	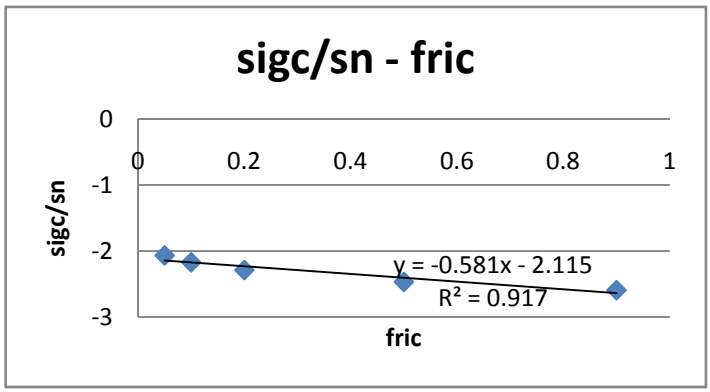
Ec/pb_Ec	<0.25	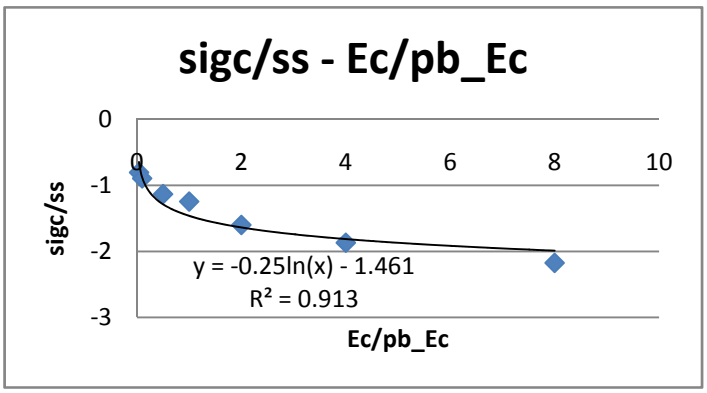
	0.25-4	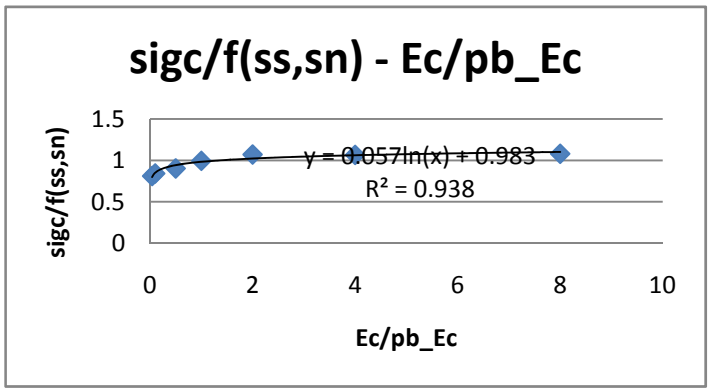

	>4	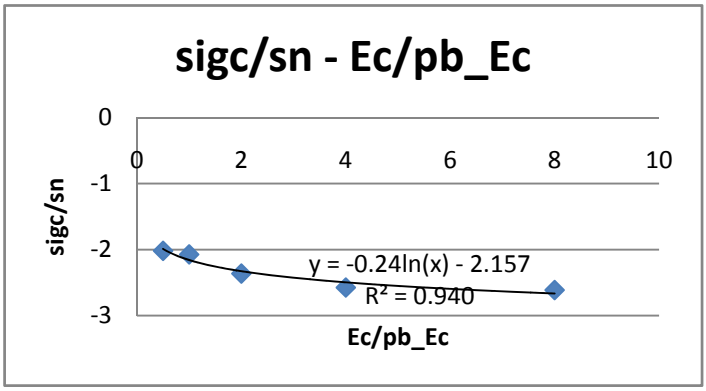

As shown in Table 4-6, the sigc/f(ss,sn) have different correlation with different micro-variables in the three ss/sn ranges. For friction, it is almost linear relation; for Ec/pb_Ec, it is logarithmic relation; for pb_kn/ks, it has linear relation in ss/sn<0.25, and logarithmic relation in other two ranges.

Table 4-7. Combined effects of micro-variables on Compressive Strength

Micro-parameter	Range of ss/sn	Graphical correlation
pb_kn/ks & friction	<0.25	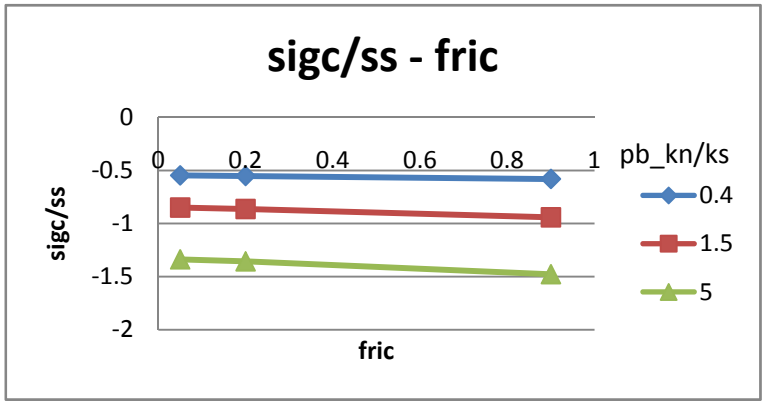

	>4	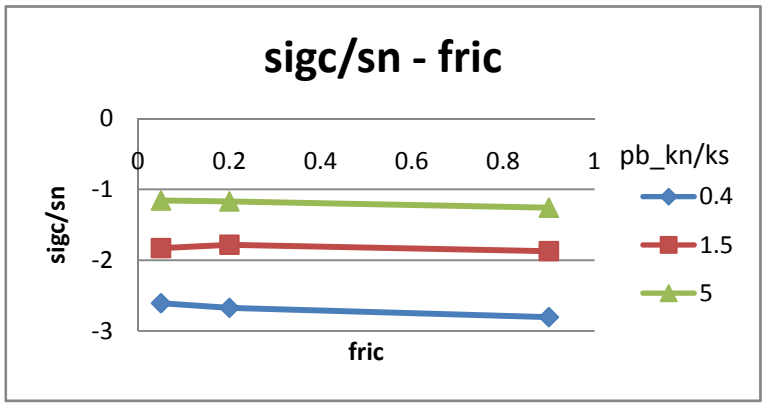
Friction & Ec/pb_Ec	<0.25	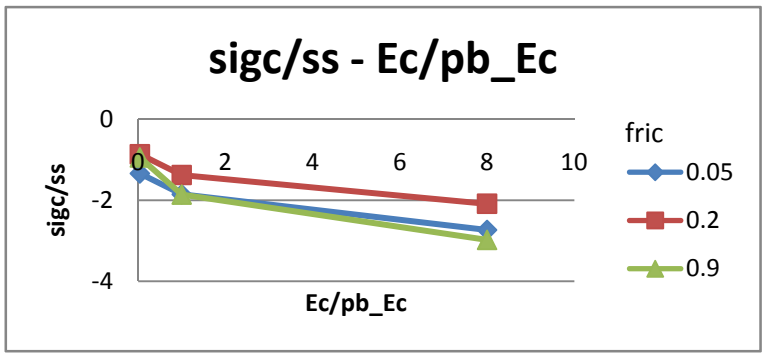
	>4	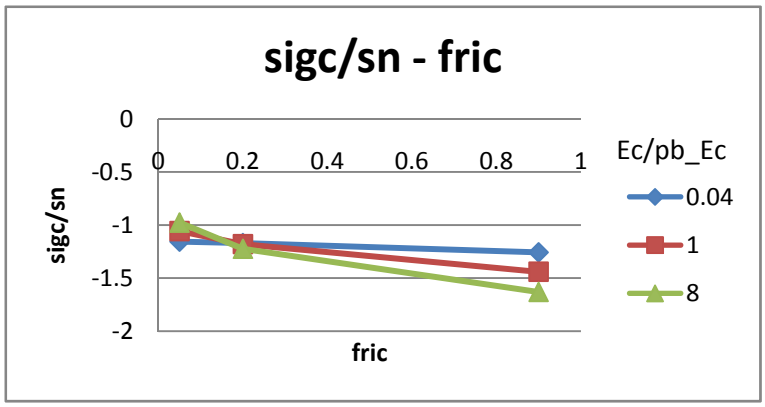
Ec/pb_Ec & pb_kn/ks	<0.25	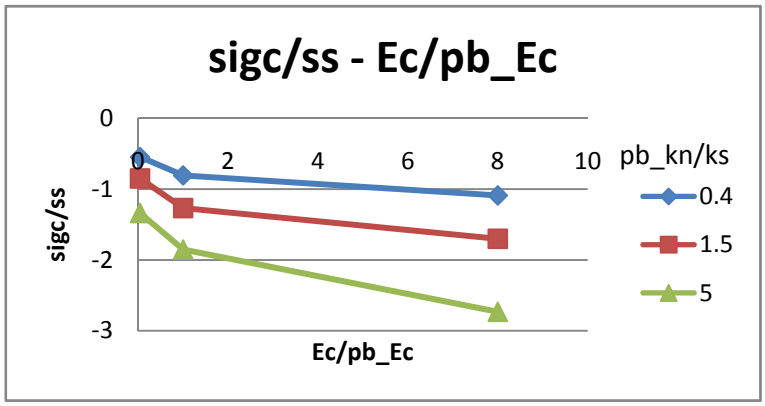

	>4	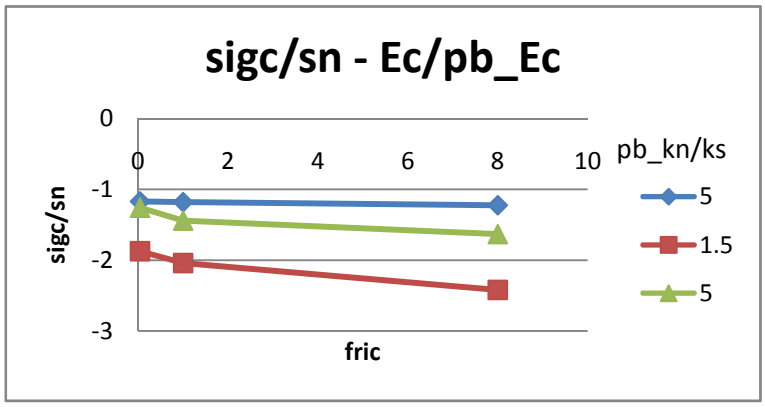

For the range <0.25 and >4, as shown in Table 4-7, the effects of Ec/pb_Ec and pb_kn/ks on sigc are independent of each other, so are the effects of pb_kn/ks and fric. For the correlation in-between on fric and E_c/pb_E_c, a slight interdependency could be found, for which a nonlinear term is introduced. And for the range 0.25-4, Compressive strength has similar individual relation with micro-variables, but the integral correlation becomes so complex that a good enough regression equation wasn't found.

Use 'Multi-linear' regression function of EXCEL to obtain the coefficients for different variables. The equations for three ss/sn ranges are shown in Table 4-8 with the determination coefficient R^2.

Table 4-8. Regression equations for compressive strength

ss/sn range	Combined Equation	R^2
<0.25	$\frac{\sigma_c}{-1.3\tau - 0.5*10^6} = 0.134 \ln \frac{\bar{k}_n}{\bar{k}_s} + 0.552\mu + 0.108 \ln \frac{E_c}{\bar{E}_c} + 0.176 \ln \frac{E_c}{\bar{E}_c} \ln \mu + 0.496$	0.933
0.25-4	$\frac{\sigma_c}{0.752\tau + 0.249\sigma - 2.2*10^6} = \Phi_2(\frac{\bar{k}_n}{\bar{k}_s}, \mu_{,c} \frac{E_c}{\bar{E}_c})$	
>4	$\frac{\sigma_c}{-2.4\sigma - 1.4*10^6} = -0.162 \ln \frac{\bar{k}_n}{\bar{k}_s} + 0.061\mu - 0.013 \ln \frac{E_c}{\bar{E}_c} + 0.117 \ln \frac{E_c}{\bar{E}_c} \ln \mu + 0.774$	0.957

4.3.4. Summary of the macro-micro regression equations

The empirical discoveries found above can be used to generate digital concrete with the required mechanical properties, although the calibration still needs to be completed step by step. The suggested procedure is in the sequence of Young's modulus -> Poisson's ratio -> Compressive strength -> other parameters. Table 4-9 for all the regression equations developed.

Table 4-9. Regression equations summary for different macro-parameters

<table>
<tr><td>Macro-Parameter</td><td colspan="4">Corresponding micro-variables and regression equation with determination coefficient</td></tr>
<tr><td rowspan="2">E</td><td>E_c</td><td>$\overline{E}_c$</td><td>$\overline{k}_n / \overline{k}_s$</td><td>$\mu$</td></tr>
<tr><td colspan="4">$\frac{E}{0.375E_c + 0.705\overline{E}_c} = -0.419\ln\frac{\overline{k}_n}{\overline{k}_s} + 0.386\mu + 1.076$, with R^2=0.929</td></tr>
<tr><td rowspan="2">ν</td><td colspan="2">$E_c / \overline{E}_c$</td><td>$\overline{k}_n / \overline{k}_s$</td><td>$\mu$</td></tr>
<tr><td colspan="4">$\nu = -0.001\frac{E_c}{\overline{E}_c} + 0.173\ln\frac{\overline{k}_n}{\overline{k}_s} - 0.158\mu + 0.0634\frac{E_c}{\overline{E}_c}\mu + 0.129$, with R^2=0.958</td></tr>
<tr><td rowspan="6">σ_c</td><td colspan="2">ss/sn<0.25</td><td>τ</td><td>μ</td></tr>
<tr><td colspan="4">$\frac{\sigma_c}{-1.3\tau - 0.5*10^6} = 0.134\ln\frac{\overline{k}_n}{\overline{k}_s} + 0.552\mu + 0.108\ln\frac{E_c}{\overline{E}_c} + 0.176\ln\frac{E_c}{\overline{E}_c}\ln\mu + 0.496$, with R^2=0.98</td></tr>
<tr><td colspan="2">0.25<ss/sn<4</td><td>τ and σ</td><td>μ</td></tr>
<tr><td colspan="4">$\frac{\sigma_c}{0.752\tau + 0.249\sigma - 2.2*10^6} = \Phi_2(\frac{\overline{k}_n}{\overline{k}_s}, \mu, _c\frac{E_c}{\overline{E}_c})$</td></tr>
<tr><td colspan="2">ss/sn>4</td><td>σ</td><td>μ</td></tr>
<tr><td colspan="4">$\frac{\sigma_c}{-2.4\sigma - 1.4*10^6} = -0.162\ln\frac{\overline{k}_n}{\overline{k}_s} + 0.061\mu - 0.013\ln\frac{E_c}{\overline{E}_c} + 0.117\ln\frac{E_c}{\overline{E}_c}\ln\mu + 0.77$, with R^2=0.917</td></tr>
</table>

Chapter 5. Simulation Results and Analysis

5.1. Visualization of DEM penetration simulation

After the generation of target and projectile models, it is convenient to assign striking velocities to the projectile and perform the impact simulation. Through PFC3D coding, a perforation test was simulated. In the process, cracking and spalling could be observed at the front face, while at the back face a much more significant scabbing is the major phenomenon.

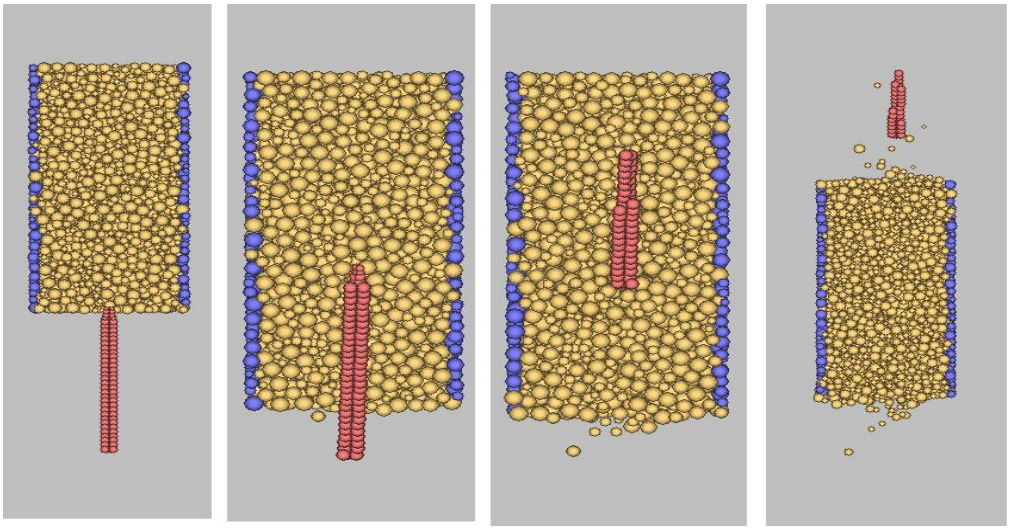

Figure 5-1. Visualization of the penetration process (with the 2nd and 3rd step enlarged)

Figure 5-1shows the concrete slab perforation process at selected time steps (with striking velocity 500m/s). In the process, cracking and spalling could be observed at the front face, while at the back face a much more significant scabbing is the major phenomenon.

Different steps correspond to different times, which can be obtained from the simulation history record, and can be used to build up the correlation with other monitored variables, such as projectile velocity, penetration depth, friction force

around the projectile, etc, as shown in Figure 5-2. These correlations could be used to analyze the mechanism of the penetration process, and compare to those from other methods.

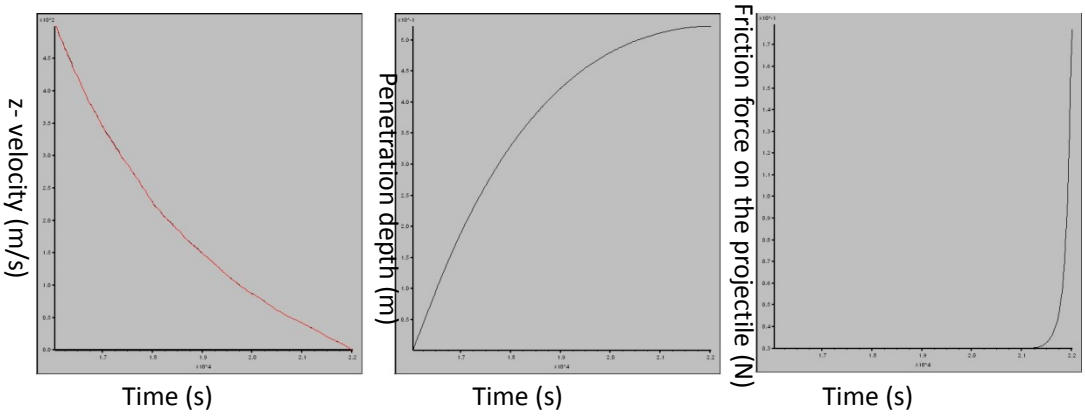

Figure 5-2. Visualization of the change of projectile velocity, penetration depth, and corresponding projectile-target friction in the penetration process

Figure 5-3, Figure 5-4, and Figure 5-5 present the time history of depth, velocity, and deceleration for a deep penetration test at impact velocity of 500 m/s, and their comparison with empirical predictions sof the third penetration case in (Forrestal, et al. 1994). As can be seen, the depth, velocity, and deceleration of the projectile vary with time non-linearly. There are similar trend and range for depth and velocity, yet the simulation has a much smaller acceleration (deceleration), which also results in a later ending point than the real test. This could probably attribute to the dynamic modulus property of the concrete, mentioned later.

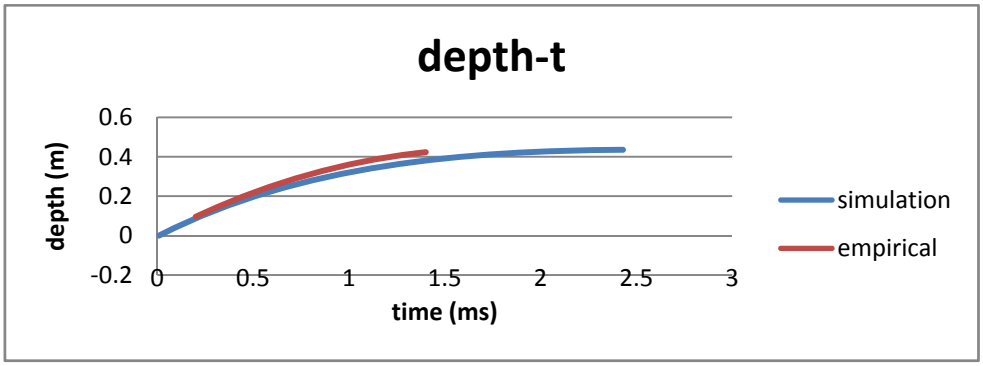

Figure 5-3. Penetration depth of the projectile for both simulation and empirical prediction

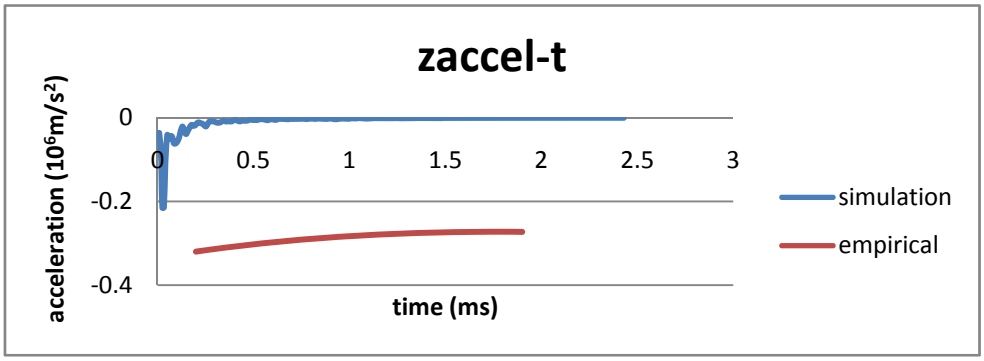

Figure 5-4. Acceleration of the projectile for both simulation and empirical prediction

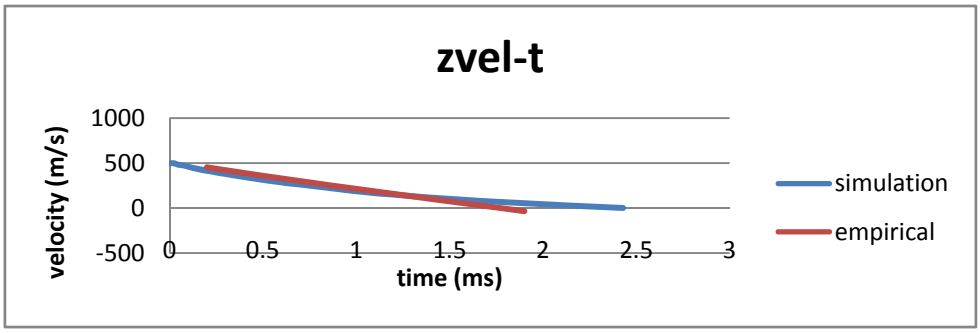

Figure 5-5. Velocity of the projectile for both simulation and empirical prediction

5.2. Velocity-Depth Test Validation and related factor analysis

The velocity-penetration depth relationship is one of the important relationships that ballistic researchers are interested in. A series of DEM simulations with the penetration at different impact velocities into a concrete target of an unconfined Compressive strength of 35MPa were conducted. This concrete is selected in order to allow comparison with experimental results and empirical correlation obtained by (Forrestal, et al. 1994).

Table 5-1 presents both the macroscopic parameters by Forrestal (1994) and the calibrated microscopic variables obtained in this study.

Table 5-2 presents the penetration depths obtained in the simulation, by the experiments, and predicted through the empirical equation, at different impact velocities.

Figure 5-6 also presents the data in the table graphically. It can be seen that DEM simulation results have a similar trend as the experimental and empirical results. However, compared to the test and Forrestal's empirical equation, the DEM simulation overestimates the penetration depth at lower velocities, and underestimates the penetration depth at higher velocities. The reason is probably because the mechanical property of concrete target is strain rate dependent, like Young's modulus which we would mention in the next section. And in this study only the static properties have been calibrated.

Table 5-1. Macro-parameters and micro-variables for the test and digital concrete

Test concrete macro-parameter	E(Pa)	v	sigc(Pa)
	28.9E+9	0.167	36.2E+6
DEM micro-variable setting	rlo (m)	Rratio	vel_cal (m/s)
	5.00E-03	2	0.01
	Iso_stress	Tol	
	-5.00E+04	0.1	
	E_c (Pa)	$\overline{E}_c$ (Pa)	$E_c / \overline{E}_c$
	300.0E+6	70E+9	0.0043
	k_n / k_s	$\overline{k}_n / \overline{k}_s$	
	1	3	
	$\overline{\sigma}_c$ (Pa)	$\overline{\tau}_c$ (Pa)	$\overline{\sigma}_c / \overline{\tau}_c$
	25E+6	50E+6	0.5
Digital concrete macro-parameter	E (Pa)	ν	σ_c (Pa)
	32E+9	0.17	36.9E+6

Table 5-2. Relation between final penetration depth and impact velocity for test, empirical equation and DEM simulation

Experiment		Empirical		Simulation
Vs	depth	Vs	depth	depth
m/s	m	m/s	m	m
277	0.173	300	0.186	0.287
410	0.31	400	0.302	0.366
431	0.411	500	0.442	0.455
499	0.48	600	0.603	0.527
567	0.525	700	0.778	0.607

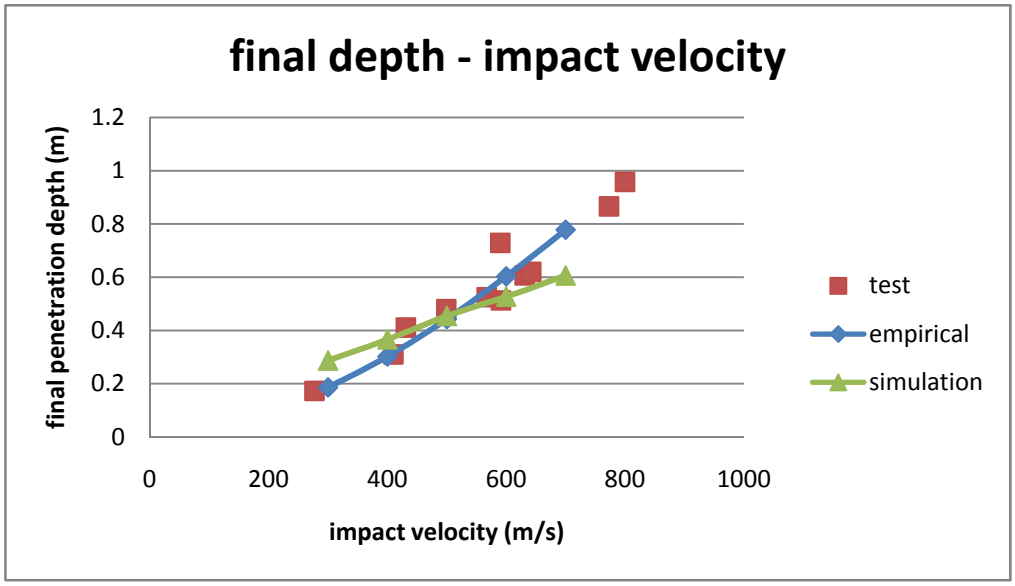

Figure 5-6. Relationship between final penetration depth and impact velocity for test, empirical equation and DEM simulation

Projectile mass plays an important role in the penetration process. The same penetration simulation as above under 500m/s was conducted, but the penetrator mass vary as 0.8kg, 0.906kg-the original one the empirical calculation uses (Forrestal, et al. 1994), and 1kg, while keeping other parameters (length, diameter) stable. The correlation between penetration depth and impact velocity is shown in Figure 5-7. It can be seen that the penetration depth increases with the increase of projectile mass. And the curve presents a close-linear correlation, with R^2 close to 1.

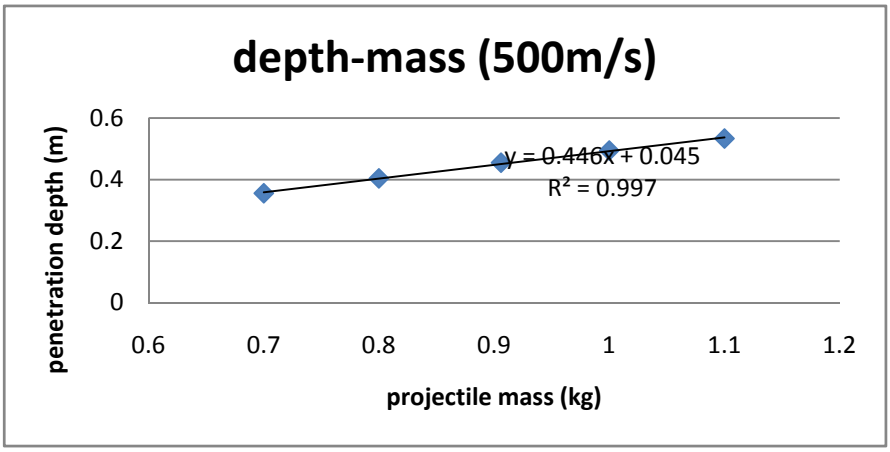

Figure 5-7. Correlation between penetration depth and projectile mass under 500m/s impact velocity

The projectile shape is another key factor for penetration process. In this part we make a study on the projectile tail diameter, varying the diameter as 0.02m, 0.024m, 0.028m-the original one the empirical calculation uses , 0.032m, and 0.036m, while keeping other parameters (length, mass) stable, as shown in Figure 5-8. It can be seen that the penetration depth decreases with the increase of projectile tail diameter, and the curve presents a close-linear relationship, with R^2 very close to 1.

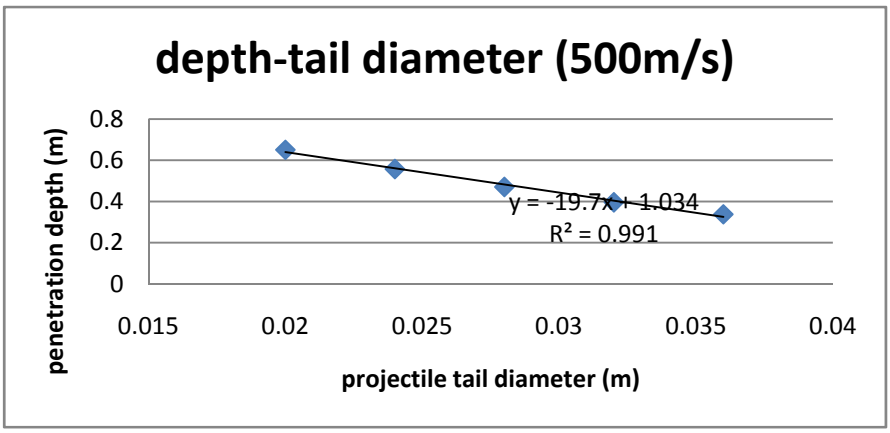

Figure 5-8. Correlation between penetration depth and projectile tail diameter under impact velocity 500m/s

As mentioned in the previous section, the interaction friction force on the

interface of concrete and projectile is determined by $f = f_{\inf} + (f_{stat} - f_{\inf})e^{-\gamma * vel}$, which is set in the projectile model. However, the friction within concrete material also plays a role in the penetration process. In the test below, we tried to make a study on this effect. As can be seen in Figure 5-9, the bigger the friction in concrete, the smaller the penetration depth. And this rule affects more at the higher velocity. However, the entire variation range is not very large. The curve presents a close-logarithmetic relationship, with R^2 very close to 1.

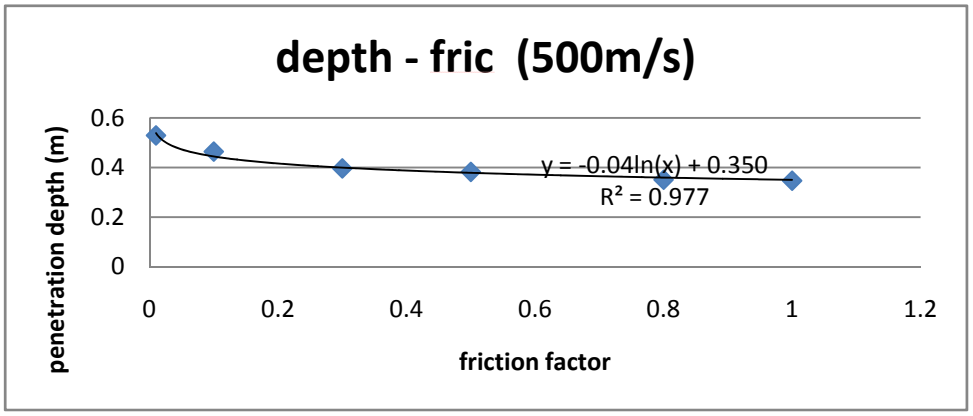

Figure 5-9. Comparison of penetration Simulation with different friction factor

5.3. Microscopic Stress and strain relationship

In order to study the constitutive relation of concrete target under dynamic loading, a cross section was chosen at 0.2m to study the relationship between stress and strain, as well as strain rate. Shown in Figure 5-10, in order to minimize the dissymmetric effect (due to the material heterogeneity), four positions at radius 0.05m on both x-axis and y-axis are selected to find the average stress, strain, stress rate and strain rate. The definition of stress and strain rate at a specific location (in PFC3D) is an average over a certain volume. Thus the radius of the measurement sphere needs to be specified, defined as 0.03m in this case. The impact velocity is 500m/s, and the values presented are the average of the four measurements in the four spheres.

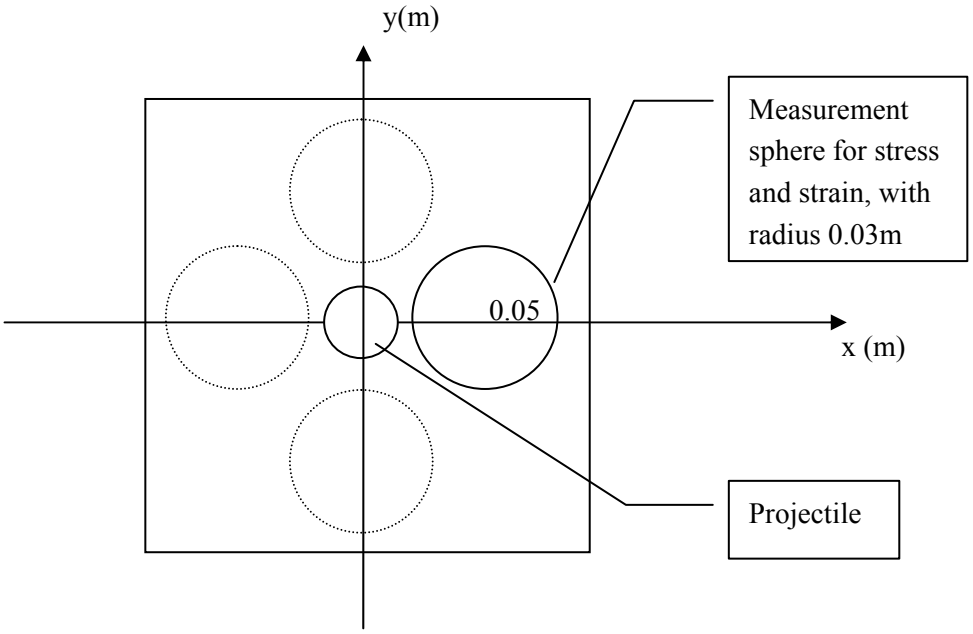

Figure 5-10. Illustration of the measurement of stress and strain

On cross-section plane z=-0.2m (the average of the four measurements on that plane)

5.3.1. Stress-strain relationship and related crack history record

Through calculation and conversion, the corresponding history of stress and strain is depicted below.

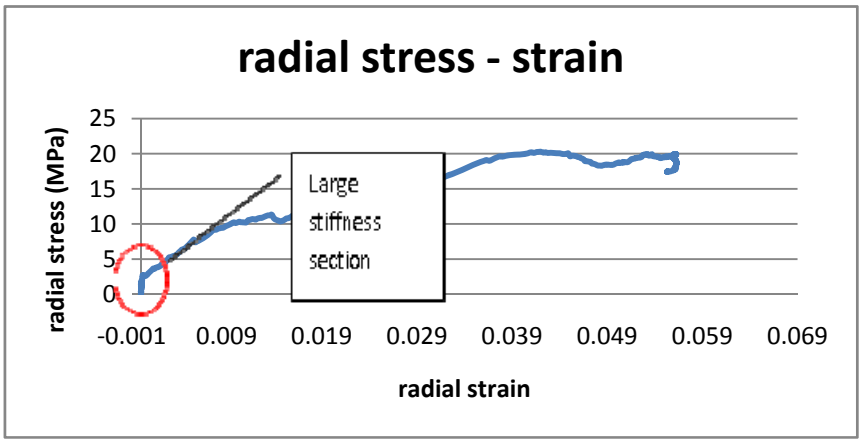

Figure 5-11. Relation between stress and strain for specified position z=-0.2m (0.25m from the projectile face) at 500m/s impact velocity

Figure 5-11 presents the radial stress-radial strain relations. Its slope is related to the elastic modulus. It can be noticed that the curve has a steep segment at first, then the slope becomes gradually smaller (smaller modulus). The reason is probably because the discrete contact model among particles consists of two parts (see the methodology section): the contact-stiffness model and the parallel-bond model. The two parts both contribute to the stiffening at first. After reaching its strength, the parallel-bond breaks, leaving only the contribution from the contact-stiffness model.

Figure 5-12, Figure 5-13, and Figure 5-14 are the crack-radial strain and time, penetration depth relationship, depicting the number of cracks (the break bonds) at different radial strains. It can be seen that an instant increase in bond breakage at the very beginning, corresponding to the stress-strain trend. It could reveal that as time goes on, the material becomes weaker, or a time delay may exist in softening the material. It should be noted that breakage of bonds includes the breakage of normal bonds and shear bonds. This information is helpful in developing damage mechanics models.

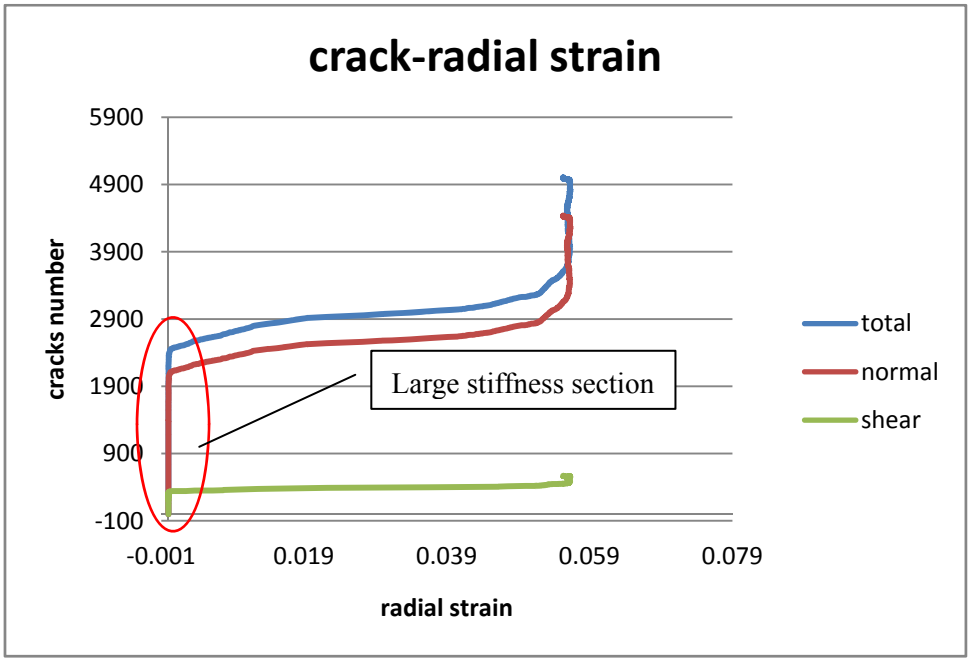

Figure 5-12. Relation between crack and radial strain at 500m/s impact velocity

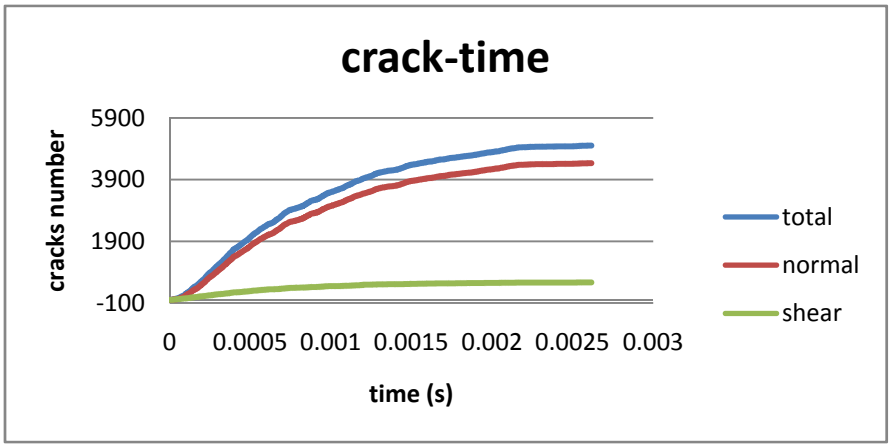

Figure 5-13. Relation between cracks number and time at 500m/s impact velocity

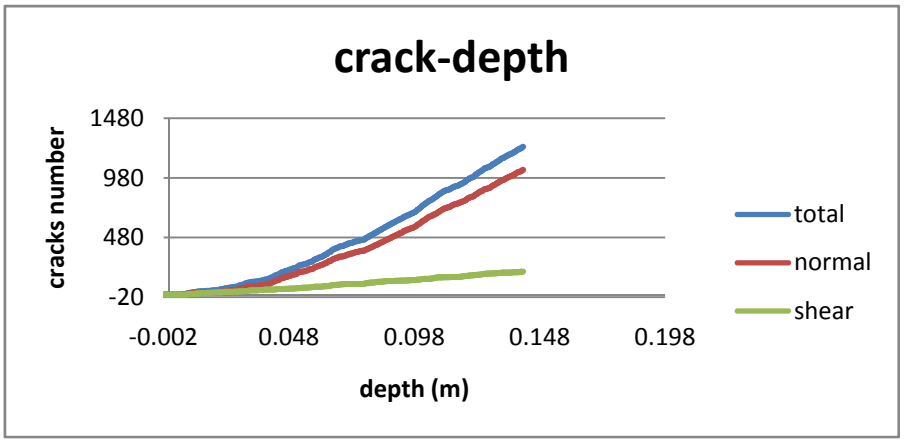

Figure 5-14. Relation between cracks number and penetration depth at 500m/s impact velocity

5.3.2. Elastic moduli – strain rate relationship analysis

To explore the relationship between the concrete modulus and strain rates, the corresponding stress-strain, stress-time, and stress-penetration depth relationship at impact velocities of 400m/s, 500m/s, 600m/s are plotted respectively.

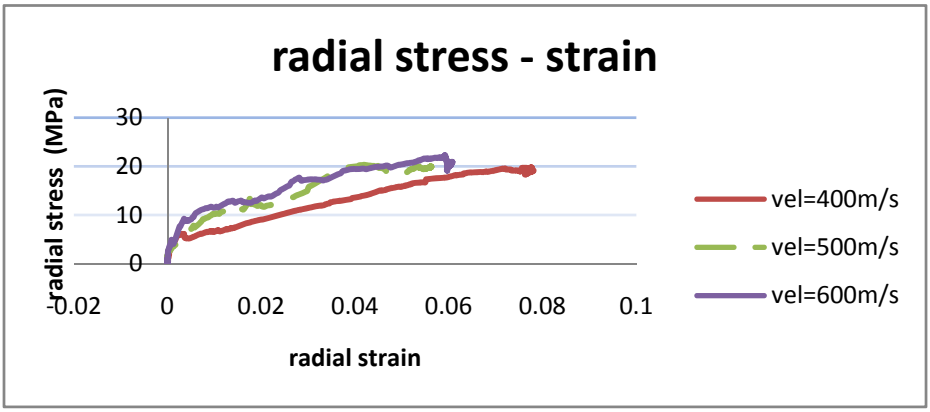

Figure 5-15. Relation between radial stress and strain

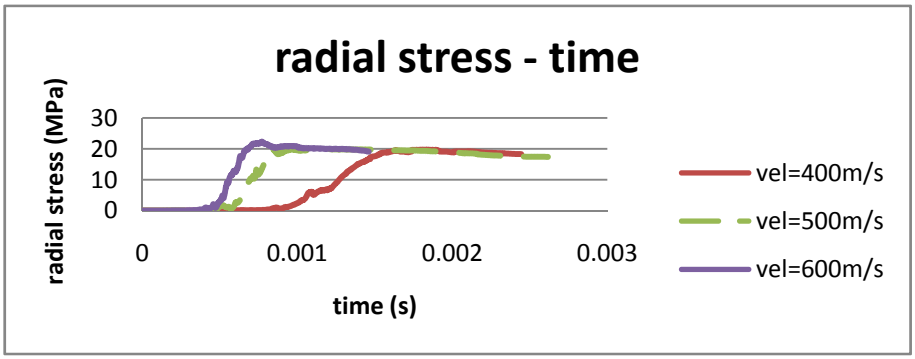

Figure 5-16. Relation between radial stress and time

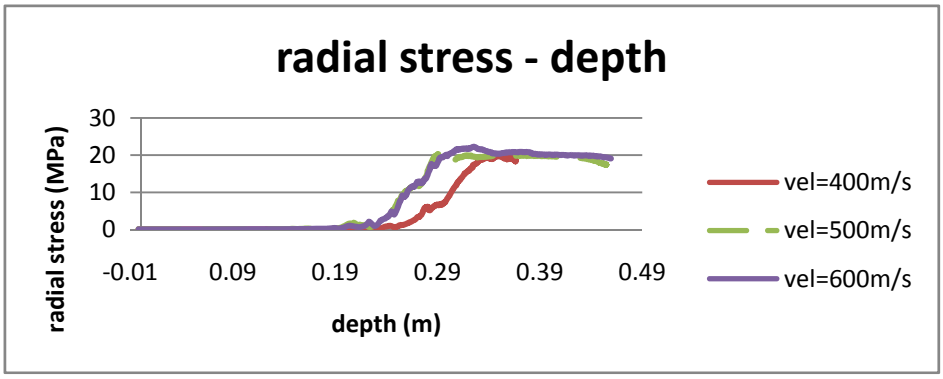

Figure 5-17. Relation between radial stress and penetration depth

As can be seen in Figure 5-15, different impact velocities induce different radial stress-strain relationships. However, the trends are similar, i.e. all have two zones of significantly different moduli, parallel-bond period and the contact-stiffness

period. This can also be reflected in Figure 5-16 and Figure 5-17, the relation between radial stress and time and penetration depth.

Figure 5-15 also shows a general trend of the slope (the modulus) of the stress-strain curves. It is steeper with the increase of the impact velocity. This slope should not be considered as the static elastic modulus (obtained from calibration tests mentioned above), but rather as the dynamic elastic modulus, which varies with strain rates.

Table 5-3 presents the relationship between the average elastic modulus (the ratio of stress over strain from the peak to the origin) and the maximum strain rate at different impact velocities. Figure 5-18 presents this relationship graphically. As can be seen, the average modulus increases with the increase of strain rate with a non-linear relationship.

Table 5-3. Relation between average elastic modulus and strain rate, with corresponding impact velocity and final penetration depth

velocity	modulus	strain rate	depth
m/s	Pa	1/s	m
400	2.54E+08	2.27E+02	0.36642
500	3.56E+08	3.11E+02	0.45483
600	3.77E+08	4.32E+02	0.52738

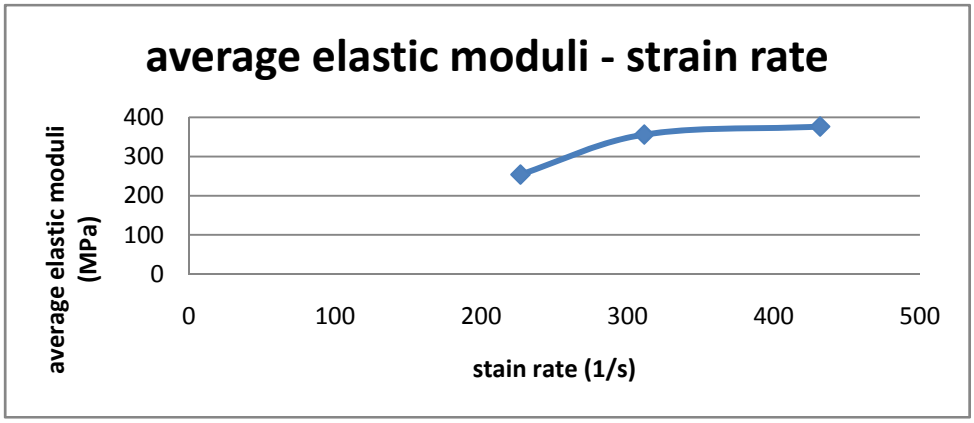

Figure 5-18. Relation between average elastic modulus and strain rate

5.3.3. Stress distribution and time relation

In order to study the stress distribution and variation with time, several locations along the radius direction in the target were selected for the stress plots. At depth 0.2m, four locations at distances 0.08m, 0.05m, 0.03m, and 0.01m away from the center of the target were selected.

For each of the four radial locations, four points, two on each of the axes, were selected for stress averaging. (Only the locations on positive x-axis are depicted, the other three measurement locations are on the positive y-axis, negative y-axis, and negative x-axis. The values used below are the average results of these four locations in order to minimize the dissymmetric effect due to the material heterogeneity.) The stress changes with time were then observed at different penetration depths of the projectile corresponding to different times, as shown in Figure 5-19 and Figure 5-20.

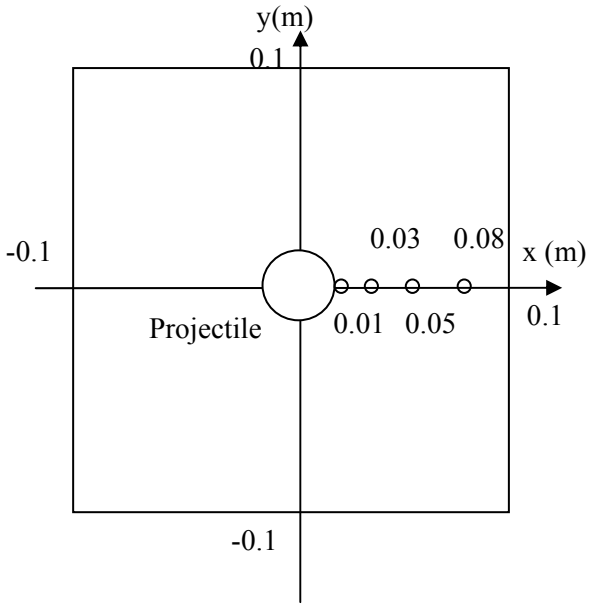

Figure 5-19. Illustration of the four measurement locations on the cross section of the target

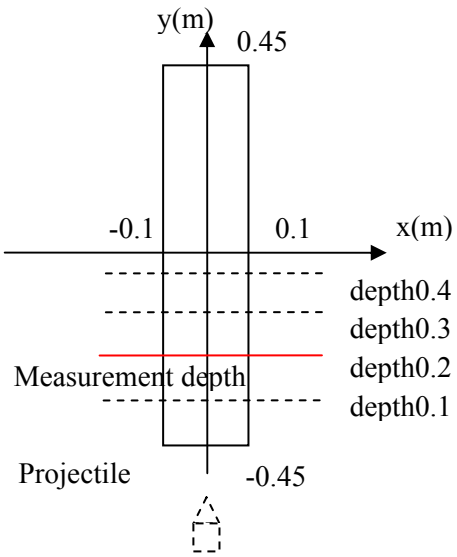

Figure 5-20. Illustration of the specified measurement depth in the target (The projectile of this illustration is not to scale)

Figure 5-21 presents the average velocity for specified radial locations at different penetration depths. It should be noted that this plot refers to the instant when the projectile tip depth reaches 0.2m. It can be seen that when projectile reaches the plane observed, the velocities of the balls on that plane are much bigger than any other time (actually balls are close to constant velocity at other times). Generally the closer the balls to the projectile, the bigger the velocities they have.

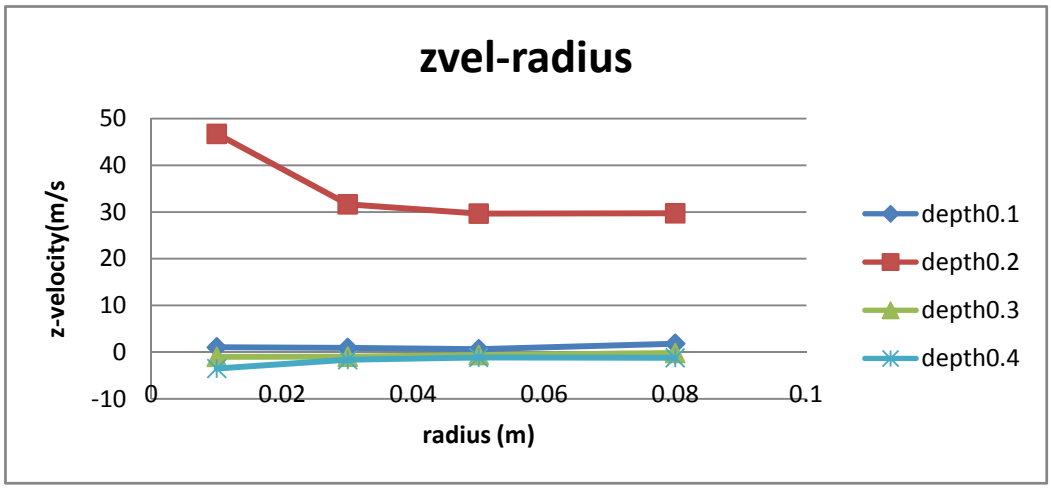

Figure 5-21. Distribution of velocity in z-direction along radius

Figure 5-22 and Figure 5-23 show the average radial stresses at the four locations. It can be seen that the locations closer to the center have bigger stress than those far away (statistically, as the microstructure, the ball configurations at the four locations may not be the same). Location wise, when the projectile tip depth reaches 0.2m, the location at 0.1m is subjected to the largest radial strain and therefore the largest stress. It should be also noted that the stress gradient is very large close to the projectile. Figure 5-23 presents the stress pulses that the four locations have felt. It can be seen that the stress pulse has a very short duration for large stress. The stress decreases sharply when away from the projectile.

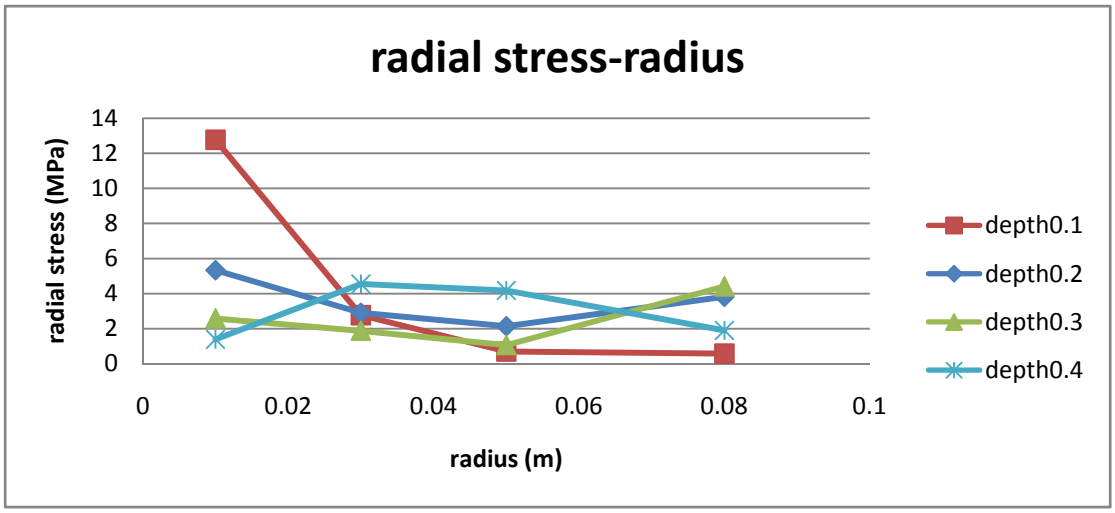

Figure 5-22. Distribution of radial stress along radius and depth

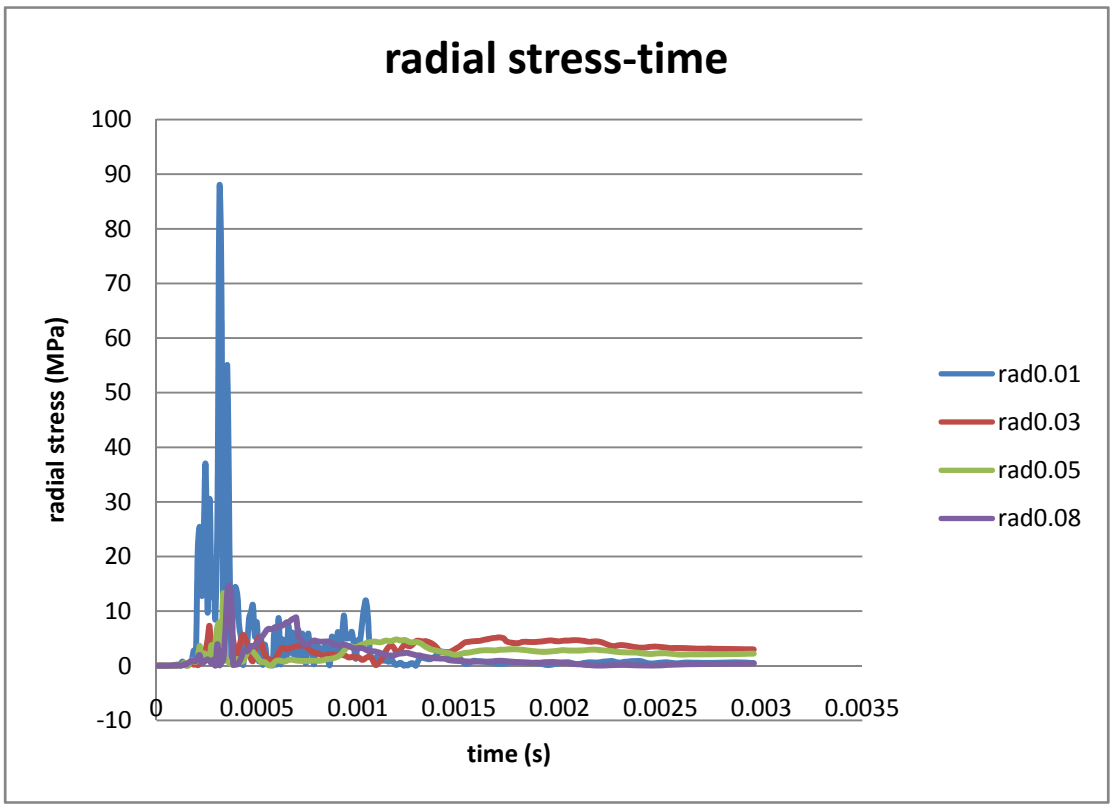

Figure 5-23. Variation of radial stress over the whole penetration process

Chapter 6. Summary and Conclusions

6.1. Scientific accomplishments

In this thesis, we applied DEM theory to build up a concrete model for simulating the normal impact penetration process. The model and conclusions developed in this thesis can be used for the next phase of integration of modeling, simulation, and experimental observations.

1. An Inverse technique and digital calibration method was developed to back-calculate the microscopic variables from the macroscopic parameters of concrete.

2. The simulation results were compared to those obtained from experimental and empirical methods. The Penetration Depths obtained from the simulations with different impact velocities compare consistently with experimental and empirical correlations.

3. The corresponding macroscopic stress – strain relations and related crack correlations were depicted to exhibit the constitutive property. We also demonstrated that modulus of elasticity of concrete is strain rate dependent, which can be obtained from the average of microscopic calculations.

4. Some major parameters, like projectile mass, size, and friction factor in concrete, were evaluated in the simulation process.

6.2. Limitation of the methodology in this thesis

The experimental equipment is still under preparation, which limits the comparison of our simulation results to the corresponding tests.

PFC3D version 3.0 limits the choice of the DEM contact models, which may not be very suitable for the concrete material. In addition, it does not have the function of developing user-defined models like the later version.

The cluster function was not utilized in the simulation discussed in this thesis. This creates difficulties for simulation of different sizes and irregular shapes of aggregate.

The calculation capacity of the lab computer disables the radius of discrete balls to further decrease, which would cause the particle number to a tremendous amount, resulting in an unacceptable calculation time.

6.3. Recommendation for the further study

Future work is planned to incorporate the actual microstructure of concrete into DEM simulations through x-ray computerized tomography imaging, image analysis and using the clustering DEM.

Integration of DEM simulation into FEM simulation and use of DEM simulation to calibrate the advanced damage mechanics models is also planned for next phase to integrate modeling, simulation and experimental observations.

References

Ai-guo, P. and H. Feng-lei (2007). "Based on Variation Method for the Shape Optimization of Penetrator Nose Shape."

Backman, M. E. and W. Goldsmith (1978). "Mechanics of penetration of projectiles into targets." International Journal of Engineering Science **16**(1): 1-99.

Bernard, R. S. (1977). Empirical Analysis of Projectile Penetration in Rock. United States**:** 23p.

Bernard, R. S. (1978). Depth and Motion Prediction for Earth Penetrators. United States**:** 31p.

Bishop, R. F., R. Hill, et al. (1945). "The theory of indentation and hardness tests." Proceedings of the Physical Society(3): 147.

Cargile, J. D. (1999). Development of a Constitutive Model for Numerical Simulation of Projectile Penetration into Brittle Geomaterials. United States**:** 227p.

Chen, E. P. (1989). "Penetration into dry porous rock: a numerical study on sliding friction simulation." Theoretical and Applied Fracture Mechanics **11**(2): 135-141.

Chen, E. P. (1994). Simulation of concrete perforation based on a continuum damage model**:** Size: 14 p.

Chen, X. W., S. C. Fan, et al. (2004). "Oblique and normal perforation of concrete targets by a rigid projectile." International Journal of Impact Engineering **30**(6): 617-637.

Chen, X. W. and Q. M. Li (2002). "Deep penetration of a non-deformable projectile with different geometrical characteristics." International Journal of Impact Engineering **27**(6): 619-37.

Cundall, P. A. and O. D. L. Strack (1979). "Discrete numerical model for granular assemblies." Geotechnique **29**(1): 47-65.

Forrestal, M. J. (1986). "Penetration into dry porous rock." International Journal of Solids and Structures **22**(12): 1485-1500.

Forrestal, M. J., B. S. Altman, et al. (1994). "Empirical equation for penetration depth of ogive-nose projectiles into concrete targets." International Journal of Impact Engineering **15**(4): 395-405.

Forrestal, M. J., D. J. Frew, et al. (1996). "Penetration of grout and concrete targets with ogive-nose steel projectiles." International Journal of Impact Engineering **18**(5): 465-476.

Forrestal, M. J., D. J. Frew, et al. (2003). "Penetration of concrete targets with deceleration-time measurements." International Journal of Impact Engineering **28**(5): 479-497.

Forrestal, M. J. and D. B. Longcope (1990). "Target strength of ceramic materials for high-velocity penetration." Journal of Applied Physics **67**(8): 3669-3672.

Forrestal, M. J. and V. K. Luk (1988). "Dynamic spherical cavity-expansion in a compressible elastic-plastic solid." Journal of Applied Mechanics, Transactions ASME **55**(2): 275-279.

Forrestal, M. J. and V. K. Luk (1992). "Penetration into soil targets." International Journal of Impact Engineering **12**(3): 427-444.

Forrestal, M. J., K. Okajima, et al. (1988). "Penetration of 6061-T651 aluminum targets with rigid long rods." Journal of Applied Mechanics, Transactions ASME **55**(4): 755-760.

Forrestal, M. J. and D. Y. Tzou (1997). "Spherical cavity-expansion penetration model for concrete targets." International Journal of Solids and Structures **34**(31-32): 4127-4146.

Frew, D. J., M. J. Forrestal, et al. (2001). "A split hopkinson pressure bar technique to determine compressive stress-strain data for rock materials." Experimental Mechanics **41**(1): 40-46.

Frew, D. J., S. J. Hanchak, et al. (1998). "Penetration of concrete targets with ogive-nose steel rods." International Journal of Impact Engineering **21**(6): 489-497.

Fu, Y., L. Wang, et al. (2008). "Quantification and simulation of particle kinematics and local strains in granular materials using X-ray tomography imaging and discrete-element method." Journal of Engineering Mechanics **134**(2): 143-154.

Goldsmith, W. (1999). "Non-ideal projectile impact on targets." International Journal of Impact Engineering **22**(2-3): 95-395.

Gomez, J. T. and A. Shukla (2001). "Multiple impact penetration of semi-infinite concrete." International Journal of Impact Engineering **25**(10): 965-979.

Henderson, D. (1976). Impact and Penetration Technology Program Parametric Study. United States**:** 138p.

Heuze, F. E. (1990). "An overview of projectile penetration into geological materials, with emphasis on rocks." International Journal of Rock Mechanics and Mining Science & Geomechanics Abstracts **27**(1): 1-14.

Huang, F., H. Wu, et al. (2005). "A numerical simulation on the perforation of reinforced concrete targets." International Journal of Impact Engineering **32**(1-4): 173-187.

Huang, H. (1999). Discrete element modeling of tool-rock interaction, University of Minnesota. **Doctor**.

Itasca Consulting Group, I. (2005). "PFC3D (Particle Flow Code in 3 Dimensions) online Manual."

Jiao, Y., X. Zhang, et al. (2007). On using discrete particle approaches for simulating the perforation process of concrete slab by hard projectile, Sanya, Hainan Island, China, Trans Tech

Publications Ltd, Stafa-Zuerich, CH-8712, Switzerland.

Kusano, N., T. Aoyagi, et al. (1992). "Impulsive local damage analyses of concrete structure by the distinct element method." Nuclear Engineering and Design **138**(1): 105-110.

Li, Q. M. and X. W. Chen (2003). "Dimensionless formulae for penetration depth of concrete target impacted by a non-deformable projectile." International Journal of Impact Engineering **28**(1): 93-116.

Liu, K., L. Gao, et al. (2004). "Application of discrete element method in impact problems." JSME International Journal, Series A: Solid Mechanics and Material Engineering **47**(2): 138-145.

Luk, V. K. and M. J. Forrestal (1987). "Penetration into semi-infinite reinforced-concrete targets with spherical and ogival nose projectiles." International Journal of Impact Engineering **6**(4): 291-301.

Luk, V. K., M. J. Forrestal, et al. (1991). "Dynamic spherical cavity expansion of strain-hardening materials." Transactions of the ASME. Journal of Applied Mechanics **58**(1): 1-6.

Magnier, S. A. and F. V. Donze (1998). "Numerical simulations of impacts using a discrete element method." Mechanics of Cohesive-frictional Materials **3**(3): 257-276.

Ng, T.-T. (1993). Numerical simulations for penetration process of concrete target using the discrete element method, New Orleans, LA, USA, Publ by ASME, New York, NY, USA.

Nishida, M., K. Tanaka, et al. (2004). "Discrete element method simulation of the restitutive characteristics of a steel spherical projectile from a particulate aggregation." JSME International Journal, Series A (Solid Mechanics and Material Engineering) **47**(3): 438-47.

Qian, L., Y. Yang, et al. (2000). "Semi-analytical model for truncated-ogive-nose projectiles penetration into semi-infinite concrete targets." International Journal of Impact Engineering **24**(9): 947-955.

Sawamoto, Y., H. Tsubota, et al. (1998). "Analytical studies on local damage to reinforced concrete structures under impact loading by discrete element method." Nuclear Engineering and Design **179**(2): 157-177.

Schoof, L. A., F. A. Maestas, et al. (1989). Numerical Method to Predict Projectile Penetration. United States**:** 6p.

Tavarez, F. A. and M. E. Plesha (2004). Discrete element method for modeling penetration, San Diego, CA, United States, American Society of Mechanical Engineers, New York, NY 10016-5990, United States.

Teland, J. A. and H. Sjol (2004). "Penetration into concrete by truncated projectiles." International Journal of Impact Engineering **30**(4): 447-464.

Tham, C. Y. (2006). "Numerical and empirical approach in predicting the penetration of a concrete

target by an ogive-nosed projectile." Finite Elements in Analysis and Design **42**(14-15): 1258-1268.

W-J.Shiu, F. Donzé, et al. (2005). "Missile impact on a concrete slab: a 3D discrete element study."

Warren, T. L. and M. R. Tabbara (1997). Spherical cavity-expansion forcing function in PRONTO 3D for application to penetration problems. Other Information: PBD: May 1997**:** Size: 27 p.

Xu, Y., L. M. Keer, et al. (1997). "Elastic-cracked model for penetration into unreinforced concrete targets with ogival nose projectiles." International Journal of Solids and Structures **34**(12): 1479-1491.

Young, C. W. (1967). Development of empirical equations for predicting depth of an earth-penetrating projectile**:** Pages: 40.

Young, C. W. (1972). Empirical Equations for Predicting Penetration Performance in Layered Earth Materials for Complex Penetrator Configurations. United States**:** 50p.

Young, C. W. (1997). Penetration equations. United States**:** 37p.

Young, C. W. (1998). Simplified analytical model of penetration with lateral loading -- User's guide. United States**:** 70p.

Zhang, D., F. Zhu, et al. (2005). "Application of beam-particle model to the problem of concrete penetration." EXPLOSION AND SHOCK WAVES **25**(1).

Zhu, F. and D. Zhang (2005). "Numerical simulation of perforation in plain concrete panel with nose shape of perforators."